

Long-term evolution of the temperature structure in magnetized protoplanetary disks and its implication for the dichotomy of planetary composition

Shoji Mori^{1,2*}, Masanobu Kunitomo^{3,4}, and Masahiro Ogihara^{5,6}

¹ Institute for Advanced Study and Department of Astronomy, Tsinghua University, Beijing 100084, China

² Astronomical Institute, Tohoku University, 6-3 Aramaki, Aoba-ku, Sendai 980-8578, Japan

³ Department of Physics, Kurume University, 67 Asahimachi, Kurume, Fukuoka 830-0011, Japan

⁴ Université Côte d’Azur, Observatoire de la Côte d’Azur, CNRS, Laboratoire Lagrange, Bd de l’Observatoire, CS 34229, 06304 Nice cedex 4, France

⁵ Tsung-Dao Lee Institute, Shanghai Jiao Tong University, 1 Lisuo Road, Shanghai 201210, China

⁶ School of Physics and Astronomy, Shanghai Jiao Tong University, 800 Dongchuan Road, Shanghai 200240, China

April 14, 2025

ABSTRACT

Context. The thermal structure and evolution of protoplanetary disks play a crucial role in planet formation. In addition to stellar irradiation, accretion heating is also believed to significantly affect the disk thermal structure and planet formation processes.

Aims. We present the long-term evolution (from the beginning of Class II to disk dissipation) of thermal structures in laminar magnetized disks to investigate where and when accretion heating is a dominant heat source. In addition, we demonstrate how the difference in disk structures affects the water content of forming planets.

Methods. We consider the mass loss by magnetohydrodynamic (MHD) and photoevaporative disk winds to investigate the influence of wind mass loss on the accretion rate profile. Our model includes the recent understanding of accretion heating; that is, the accretion heating in the laminar disks is less efficient than that in turbulent disks because of surface heating at optically thinner altitudes and energy removal by disk winds.

Results. We find that the accretion heating is weaker than irradiation heating at around 1–10 au even in the early Class II disk, whereas it can affect the temperature in the inner 1-au region. We also find that the MHD-wind mass loss in the inner region can significantly reduce the accretion rate compared with that in the outer region, in turn reducing accretion heating. Furthermore, using evolving disk structures, we demonstrate that updating accretion heating models impacts the evolution of protoplanets. In particular, we find that our model may produce a dichotomy of the planetary water fraction of 1–10 M_{\oplus} .

Key words. Accretion, accretion disks – Protoplanetary disks – Magnetohydrodynamics (MHD) – Planets and satellites: formation – Planets and satellites: composition

1. Introduction

The temperature structure in protoplanetary disks (PPDs) impacts many aspects of planet formation. The disk temperature determines the location of the water snowline (e.g., Hayashi et al. 1979; Oka et al. 2011; Morbidelli et al. 2016; Chambers 2023; Wang et al. 2025) and the water content of the forming terrestrial planets (e.g., Raymond et al. 2005; Mulders et al. 2013; Sato et al. 2016; Ida et al. 2019; Venturini et al. 2020; Izidoro et al. 2021). In addition, the temperature affects planetary formation processes, such as, the halting of pebble accretion onto protoplanets (i.e., pebble isolation; e.g., Lambrechts et al. 2014; Lambrechts & Johansen 2014; Bitsch et al. 2015), the mass of objects formed via streaming instability (e.g., Schäfer et al. 2017; Liu et al. 2020), and the gas-giant migration rate and gap forming mass (e.g., Lin & Papaloizou 1979; Goldreich & Tremaine 1979; Tanaka et al. 2002; Paardekooper et al. 2010; Kanagawa et al. 2018).

Whereas the temperature profile in the outer region is determined by irradiation heating, the inner profile is deviated by accretion heating. The former is due to stellar irradiation, while the latter mechanism is due to the energy released through mass accretion. In classical disk models, the disk is assumed to be turbulent; thus, turbulent viscosity causes energy dissipation in accretion heating (i.e., viscous heating; Shakura & Sunyaev 1973; Lynden-Bell & Pringle 1974). The heat produced by viscous heating is released around the midplane, which we refer to as midplane heating. When the disk is optically thick for radiative cooling from the midplane heat, the heat accumulates in the disk, and it may efficiently increase the disk temperature (*blanketing effect*; see Hubeny 1990; Nakamoto & Nakagawa 1994; Oka et al. 2011; Savvidou et al. 2020).

Nevertheless, the presence of strong disk turbulence is doubtful. Magnetorotational instability (MRI; Balbus & Hawley 1991) may generate vigorous turbulence, but it is suppressed by nonideal magnetohydrodynamic (MHD) effects (i.e., Ohmic diffusion, ambipolar diffusion, and Hall effect) in weakly ionized gas of PPDs (e.g., Gammie 1996; Sano & Stone 2002; Perez-Becker & Chiang 2011; Bai & Stone 2013; Bai 2013; Gressel et al. 2015; Bai 2017; Iwasaki et al. 2024). Disk obser-

* e-mail: mori.s@astr.tohoku.ac.jp

variations also suggest the absence of strong turbulence in the disk interior (see the review of Rosotti 2023).

Therefore, instead of turbulent disks, laminar disk models with accretion driven by global-scaled magnetic fields have attracted attention. The stress of magnetic fields threading the disk removes the angular momentum from the disk through disk winds (e.g., Blandford & Payne 1982; Shibata & Uchida 1986; Kudoh & Shibata 1995; Suzuki & Inutsuka 2009; Bai & Stone 2013; Bai 2013; Bai et al. 2016), referred to as wind-driven accretion. If there is sufficient magnetic flux, this mechanism efficiently drives disk accretion and may result in accretion rates that align with observational data (e.g., Suzuki et al. 2016; Bai 2016; Tabone et al. 2020; Lesur 2021; Tabone et al. 2022; Weder et al. 2023).

Accretion heating in magnetic laminar disks is less efficient than that in classical turbulent disks (see Figure 1). Nonideal MHD simulations (Hirose & Turner 2011; Mori et al. 2019) have shown that the accretion energy stored in magnetic fields dissipates apart from the midplane. The heat is released in optically thinner regions, and thus the cooling is more efficient. Mori et al. (2021) (hereafter referred to as M21) modeled the surface heating (Mori et al. 2019) and demonstrated that accretion heating can be remarkably inefficient. Kondo et al. (2023) updated the M21 model by considering dust growth and showed that it increased the ionization fraction with a higher opacity, resulting in a somewhat higher impact of accretion heating than that of M21.

Although the previous studies have simplified the treatment of the accretion rate (M21; Kondo et al. 2023), this simplification may affect the temperature structure. They assumed a uniform distribution of the accretion rate by neglecting the mass loss. The strong disk mass loss can affect the accretion rate. Moreover, the evolution of the accretion rate was assumed to follow the observational relationship between the stellar accretion rate and age. However, the accretion rate evolution of an individual object does not necessarily follow the observational relation obtained from numerous stars.

In this study, we calculate the long-term evolution of the temperature structure in laminar magnetized PPDs, with the mass loss by MHD and photoevaporative winds. This allows us to evaluate the impact of the simplification made in previous studies. Additionally, whereas previous studies focused on the temperature structure around 1 au and snowline migration, we pose a more general question: where and when does accretion heating influence disk temperature? We define the region where accretion heating dominates as the *accretion-heated region*, where temperature depends on factors such as the accretion rate, dust opacity, and ionization fraction. Outside this region, the temperature can be approximated by conventional passively heated disk models.

Furthermore, we investigate how the disk temperature structure influences planetary evolution, with a particular focus on water content. Recent exoplanet observations have revealed a dichotomy in the volatile composition of close-in planets within the range of 1–10 M_{\oplus} (Luque & Pallé 2022; Parviainen et al. 2024; Parc et al. 2024). Specifically, according to Parc et al. (2024), volatile-rich planets are found above 4.2 M_{\oplus} around FG-type stars. Rogers et al. (2025) estimated that the water fraction of super-Earths is less than a few %. The migration of planets that form beyond the snowline plays a significant role in shaping their compositions (e.g. Venturini et al. 2020; Izidoro et al. 2021, 2022; Burn et al. 2024). In this work, we explore how planetary growth and migration shape the dichotomy in planetary water content, based on different disk mod-

els. Although processes such as planet photoevaporation (e.g., Owen & Wu 2013, 2017; McDonald et al. 2019; Affolter et al. 2023) and core-powered mass loss (e.g. Ginzburg et al. 2018; Gupta & Schlichting 2019), which release hydrogen after migration, may also influence the water content, a comprehensive analysis incorporating these effects is left for future study.

This paper is organized as follows. In Section 2, we describe the methodology and models used in the one-dimensional disk evolution simulation. Section 3 presents the simulation results, focusing on the accretion-heated region. We also perform parameter studies. In Section 4, we describe the updates from previous works and discuss the impact of the thermal structure on the evolution process and water fraction of protoplanets.

2. Method

In this study, we designed the disk model to be a wind-driven accretion disk (see Section 2.1 for the basic equations) with the mass loss (Section 2.3). Accretion is mainly driven by the removal of the angular momentum by wind stress, and weak radial stress is also considered.

For the thermal structure, we consider two heating models, as depicted in Figure 1: MHD heating and classical viscous heating (see Section 2.2). Our MHD heating model considers surface heating depending on the vertical profile of the ionization fraction. The energy loss and mass loss by the disk winds are also considered. The later model, the classical viscous heating model, corresponds to the “Weak DW” case in Suzuki et al. (2016). In this model, heating takes place at the midplane. Although the energy-loss and mass-loss by the disk winds may happen, their strengths are weak. The difference in the two models highlights the update from the conventional viscous-heated disks.

As an update from M21, we selected simulation parameters based on the median values of plausible disk parameters to derive a representative temperature structure in our model. This contrasts with M21, which chose parameters to maximize accretion heating. For the energy fraction of accretion heating, ϵ_{rad} , we adopt a typical value suggested by MHD simulations (see Sections 2.2 and 2.4). Additionally, we update the stellar luminosity evolution (see Section 2.2.2).

2.1. Basic equation

We solve the one-dimensional advection–diffusion equation for surface density (e.g., Lynden-Bell & Pringle 1974; Suzuki et al. 2016; Kunitomo et al. 2020):

$$\frac{\partial \Sigma}{\partial t} - \frac{1}{r} \frac{\partial}{\partial r} \left[\frac{2}{r\Omega} \left\{ \frac{\partial}{\partial r} (r^2 \Sigma \alpha_{r\phi} c_s^2) + r^2 \alpha_{\phi z} (\rho c_s^2)_{\text{mid}} \right\} \right] + \dot{\Sigma}_{\text{MDW}} + \dot{\Sigma}_{\text{PEW}} = 0, \quad (1)$$

where Σ is the gas surface density, t is the time, r is the distance from the central star, ρ is the gas density, the subscript “mid” stands for the midplane, $\dot{\Sigma}_{\text{MDW}}$ is the MHD wind mass loss rate, and $\dot{\Sigma}_{\text{PEW}}$ is the photoevaporation rate. The midplane sound speed c_s is given by the midplane temperature T_{mid} as $c_s = \sqrt{k_B T_{\text{mid}} / (\mu m_u)}$, where k_B is the Boltzmann constant, $\mu = 2.34$ is the mean molecular weight, and m_u is the atomic mass. The gas scale height is $H = c_s / \Omega$, where $\Omega = \sqrt{GM_{\star} / r^3}$, with G being the gravitational constant and M_{\star} being the stellar mass. The midplane density is given by $\rho_{\text{mid}} = \Sigma / (\sqrt{2\pi} H)$. We neglect here the disk self-gravity and pressure-gradient forces. We use the same numerical scheme as Kunitomo et al. (2020) to

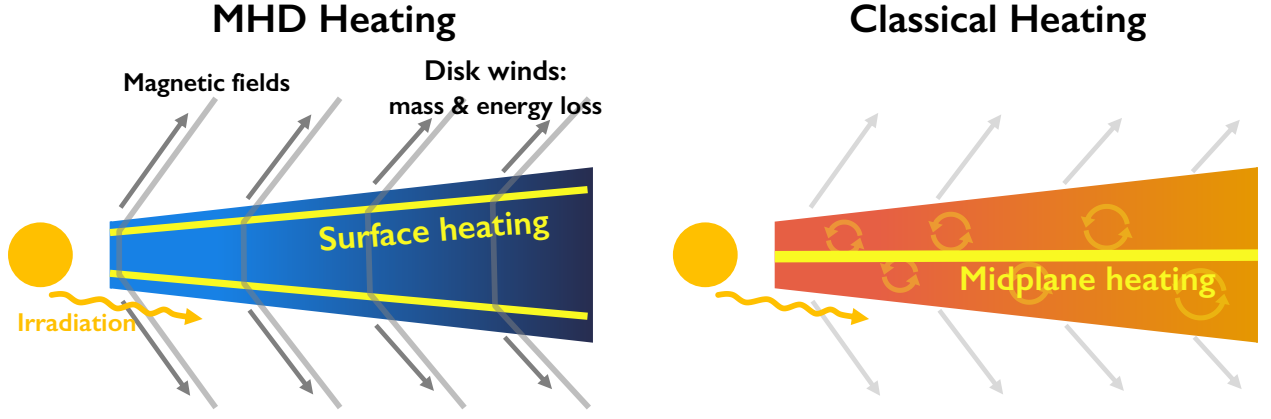


Fig. 1. Schematic picture of the two heating models shown in this paper: MHD heating and classical heating. The MHD heating model includes the effects where (1) accretion heating occurs at a high altitude, (2) the accretion energy is taken by disk winds, and (3) the accretion rate is reduced by the mass loss of the winds. In the classical heating model, accretion heating occurs at midplane, and the (2)–(3) wind effects are weak. Both models include irradiation heating.

solve Equation (1) (e.g., grid spacing, explicit code, and boundary conditions).

The terms $\overline{\alpha_{r\phi}}$ and $\overline{\alpha_{\phi z}}$ in Equation (1) are responsible for the radial mass flow due to the radial and vertical angular momentum transport, respectively. These two parameters model the strength of the radial and vertical stresses as

$$\int dz \left(\rho v_r \delta v_\phi - \frac{B_r B_\phi}{4\pi} \right) \equiv \overline{\alpha_{r\phi}} \Sigma c_s^2, \quad (2)$$

$$\left(\rho \delta v_\phi v_z - \frac{B_\phi B_z}{4\pi} \right)_w \equiv \overline{\alpha_{\phi z}} \rho_{\text{mid}} c_s^2, \quad (3)$$

where \mathbf{B} represents the magnetic field, \mathbf{v} indicates the velocity, and δv_ϕ is the deviation from the Keplerian velocity. The parenthesis with the subscript “w” conducts the division between the values at the top and bottom of the wind base. The choice of these parameter values is described in Section 2.4.

2.2. Temperature structure

As shown in Figure 1, we consider the MHD heating model and classical heating model. In both models, the midplane temperature T_{mid} is given by

$$T_{\text{mid}} = (T_{\text{acc}}^4 + T_{\text{irr}}^4)^{1/4}, \quad (4)$$

where T_{acc} and T_{irr} are the midplane temperatures solely due to accretion heating and irradiation heating, respectively. The contribution by accretion heating, T_{acc} , depends on the heating model. The treatment of T_{irr} is common between the two heating models (see Section 2.2.2).

2.2.1. Accretion heating

For the MHD heating and classical models, we give T_{acc} by following M21 (see their Appendix A):

$$T_{\text{acc}} = \left[\left(\frac{3F_{\text{rad}}}{8\sigma} \right) \left(\kappa \Sigma_{\text{heat}} + \frac{1}{\sqrt{3}} \right) \right]^{1/4}, \quad (5)$$

where F_{rad} is the energy flux that escaped as radiation from the disk, σ is the Stefan–Boltzmann constant, Σ_{heat} is the column density above the heating layer, κ is the Rosseland-mean opacity for the radiation from the disk, and the term in the optically

thin region is neglected. We adopt a simple opacity model as a function of T_{mid} , similar to Kunitomo et al. (2020):

$$\kappa = \kappa_0 \left[1 + \exp \left(\frac{T_{\text{mid}} - T_{\text{sub}}}{\Delta T/2} \right) \right]^{-1} \min \left[1, \left(\frac{T_{\text{mid}}}{170 \text{ K}} \right)^2 \right], \quad (6)$$

where the reference Rosseland-mean opacity κ_0 is set to $5 \text{ cm}^2 \text{ g}^{-1}$, $T_{\text{sub}} = 1500 \text{ K}$ and $\Delta T = 150 \text{ K}$.

We vary Σ_{heat} depending on the heating model. In the classical heating model, the heating takes place at the midplane; thus, we set Σ_{heat} to be $\Sigma/2$. In the MHD heating model, we give Σ_{heat} as the mass column density Σ_{Am} , where the ambipolar Elsasser number Am is a critical value (see M21, for details). Here, we take the critical value to be 0.3 as in M21. This approach is based on the simulation results where the accretion heating occurs at the thin layer where $\text{Am} \sim 1$ (see Figure 1 of Mori et al. (2019)). To obtain the vertical Am distribution for each radius, we calculate the ionization fraction along the vertical direction by assuming hydrostatic equilibrium and then calculate Am , as in M21 (see also Mori & Okuzumi 2016).

We parameterize the total heating rate F_{rad} by the fraction ϵ_{rad} of the dissipated energy in the generated energy, as in Suzuki et al. (2016):

$$F_{\text{rad}} = \epsilon_{\text{rad}} (\Gamma_{r\phi} + \Gamma_{\phi z}) \quad (7)$$

where $\Gamma_{r\phi}$ and $\Gamma_{\phi z}$ are, respectively, the liberated energy due to the $r\phi$ - and ϕz -component stresses. These are calculated by

$$\Gamma_{r\phi} = \frac{3}{2} \Omega \Sigma \overline{\alpha_{r\phi}} c_s^2, \quad (8)$$

$$\Gamma_{\phi z} = r \Omega \overline{\alpha_{\phi z}} \rho_{\text{mid}} c_s^2. \quad (9)$$

2.2.2. Irradiation heating

We consider two regimes for the midplane temperature due to irradiation, depending on the optical depth of the stellar direct radiation. In the optically thick region, according to Kusaka et al. (1970) and Chiang & Goldreich (1997),

$$T_{\text{irr,thick}} = 110 \text{ K} \left(\frac{r}{\text{au}} \right)^{-3/7} \left(\frac{L_\star}{L_\odot} \right)^{2/7} \left(\frac{M_\star}{M_\odot} \right)^{-1/7}, \quad (10)$$

where L_\star is the stellar luminosity, and half of the stellar hemisphere is assumed to illuminate the disk surface. When the disk

is optically thin for the stellar light through the midplane, we give (Hayashi 1981),

$$T_{\text{irr,thin}} = 280 \text{ K} \left(\frac{r}{\text{au}} \right)^{-1/2} \left(\frac{L_\star}{L_\odot} \right)^{1/4}. \quad (11)$$

We switch these regimes using the irradiation optical depth ($\tau_\star(r) = \int_0^r \kappa_\star \rho_{\text{mid}} dr'$) along the midplane, where κ_\star is the Planck-mean opacity for the stellar light:

$$T_{\text{irr}}^4 = T_{\text{irr,thin}}^4 + T_{\text{irr,thick}}^4 \exp(-\tau_\star). \quad (12)$$

Here, we set $\kappa_\star = 10 \text{ cm}^2 \text{ g}^{-1}$, but the results are insensitive to this value. In addition, a gradual temperature transition (e.g., Oka et al. 2011; Okuzumi et al. 2022) is not considered. However, the intermediate state would appear only in a short timescale because the surface density is quickly dropped by photoevaporation.

In this paper, we use a more realistic evolution model of stellar luminosity L_\star than that of M21, where the L_\star evolution model is the same as that in Feiden (2016). We also adopt the model in Feiden (2016) but with a modification: as the initial luminosity in their model is higher than expected from those of star formation models, we shift $t = 0$ to the timing when an evolutionary track on the Hertzsprung–Russell diagram crosses the birthline of Stahler & Palla (2004, see also Figure 1 of Kunitomo et al. 2021). As shown later, the luminosity in the early phase ($t \lesssim 0.5 \text{ Myr}$) is lower than that used in M21, leading to the earlier arrival of the snowline at 1 au ($\approx 0.2 \text{ Myr}$).

2.3. MHD and photoevaporative winds

For the mass loss by MHD disk wind, we follow the approach in Suzuki et al. (2016). The mass-loss rate is parameterized as $C_w \equiv \dot{\Sigma}_{\text{MDW}}/(\rho_{\text{mid}} c_s)$, which is the mass flux normalized by $\rho_{\text{mid}} c_s$. In this model, the mass-loss parameter C_w is given by a constant $C_{w,0}$ unless an energy constraint of the disk winds is violated. The energy constraint is given from the primary energy balance (Suzuki et al. 2016):

$$\dot{\Sigma}_{\text{MDW}} (E_w + r^2 \Omega^2 / 2) + F_{\text{rad}} \approx \Gamma_{r\phi} + \Gamma_{\phi z}, \quad (13)$$

where E_w is the specific energy density of the magnetic disk wind. To launch the disk wind, the wind's energy E_w must be positive. Using Equation (7), we have the constraint

$$C_w \gtrsim \frac{2(1 - \epsilon_{\text{rad}})(\Gamma_{r\phi} + \Gamma_{\phi z})}{\rho_{\text{mid}} c_s r^2 \Omega^2} \equiv C_{w,e}, \quad (14)$$

where $C_{w,e}$ is the mass-loss parameter required from the energy constraint. We assume here that the energy balance due to irradiation heating is independently satisfied. The irradiation heating rate and its cooling rate are, thus, not seen. For $C_{w,0}$, we adopt the same value in Suzuki et al. (2016). Although the mass-loss rate may vary with different simulations, we adopt $C_{w,0} = 10^{-5}$ used in Suzuki et al. (2016). Thus, we give the mass loss rate of the MHD disk wind as

$$\dot{\Sigma}_{\text{MDW}} = \max(C_{w,0}, C_{w,e}) \rho_{\text{mid}} c_s. \quad (15)$$

Note that although C_w depends on the magnetic flux threading the disk (e.g., Bai & Stone 2013; Bai 2013, 2017; Lesur 2021), this dependence is not considered in this study.

Table 1. Common parameter values.

Parameter	Value
Radius of the inner boundary, r_{in}	0.01 au
Radius of the outer boundary	10^4 au
Viscosity parameter, $\overline{\alpha_{r\phi}}$	10^{-4}
Initial disk mass	$0.2 M_\star$
Initial characteristic radius, r_c	100 au
Slope of initial surface density, p	-1
Reference opacity, κ_0	$5 \text{ cm}^2 \text{ g}^{-1}$

Table 2. Disk models considered in Section 3.

Name	Σ_{heat}	ϵ_{rad}	$\overline{\alpha_{\phi z}}$	f_{dg}
Fid	Σ_{Am}	0.1	const	0.01
Vis	$\Sigma/2$	0.9	const	N/A
eps001	Σ_{Am}	0.01	const	0.01
eps1	Σ_{Am}	1.0	const	0.01
DG	Σ_{Am}	0.1	const	0.001
apz-sgm	Σ_{Am}	0.1	Σ -dep	0.01

Notes. The column density for the accretion heating, Σ_{heat} , is taken at either the midplane ($\Sigma/2$) or at the altitude where $\text{Am} = 0.3$ (Σ_{Am}). The model of $\overline{\alpha_{\phi z}}$ is either a constant value of 10^{-3} (const) or depends on Σ (Σ -dep). The dust-to-gas ratio f_{dg} is used only for the ionization fraction calculation, while the Rosseland-mean opacity κ in the temperature calculation is given by Equation (6).

Furthermore, we consider mass loss through photoevaporation. Young protostars are active and emit intense extreme ultraviolet (EUV), far ultraviolet (FUV), and X-rays. When exposed to such energetic rays, the gas in the upper disk becomes so hot that it exceeds the escape velocity from the stellar gravitational potential and flows out of the disk. For the photoevaporative mass-loss rate $\dot{\Sigma}_{\text{PEW}}$, we follow Kunitomo et al. (2020, see their Sect. 2.4): we consider X-ray ($\dot{\Sigma}_{\text{X}}$) and EUV ($\dot{\Sigma}_{\text{EUV}}$) photoevaporation rates in the literature (Alexander et al. 2006; Alexander & Armitage 2007; Owen et al. 2012) with the X-ray luminosity of 10^{30} erg/s and EUV luminosity of 10^{41} s^{-1} , and their sum is the mass-loss rate $\dot{\Sigma}_{\text{PEW}}$:

$$\dot{\Sigma}_{\text{PEW}} = \dot{\Sigma}_{\text{X}} + \dot{\Sigma}_{\text{EUV}}. \quad (16)$$

Once a gap opens, since the inner disk accretes rapidly onto the star and the outer disk is directly irradiated, we switch $\dot{\Sigma}_{\text{PEW}}$ as in Kunitomo et al. (2020). We note that although $\dot{\Sigma}_{\text{PEW}}$ is still actively studied and uncertain (see, e.g., discussions in Section 5.4 of Kunitomo et al. 2021) (see also Wang & Goodman 2017; Picogna et al. 2019; Komaki et al. 2021; Nakatani et al. 2024), this does not affect the conclusion of this study.

2.4. Simulation settings and parameter choice

In Table 1, we summarize the values for the common parameters throughout this paper. Table 2 presents the parameter set in the fiducial model (Fid) and summarizes the other models used in this paper. For all runs, the calculation is performed until $t = 10 \text{ Myr}$, which is sufficiently longer than the typical disk lifetime.

For the initial condition of the surface density, we give Σ with the form $\Sigma \propto (r/\text{au})^p \exp(-r/r_c)$, where the characteristic radius r_c is set to 100 au and p is set to -1. The initial disk mass is set to $0.2 M_\star$ in the fiducial setting.

The parameters on the accretion stress ($\overline{\alpha_{\phi z}}$ and $\overline{\alpha_{r\phi}}$; Equations (2) and (3)) are given to express the case where wind stress

dominates over turbulent stress. In the model **Fid**, we set $\overline{\alpha_{\phi z}}$ to be a constant ($\overline{\alpha_{\phi z}} = 10^{-3}$) and $\overline{\alpha_{r\phi}}$ to be $\overline{\alpha_{r\phi}} = 10^{-4}$.

In reality, the $\overline{\alpha_{\phi z}}$ value is related to the magnetic flux transport in the disk, which is still highly uncertain. [Suzuki et al. \(2016\)](#) considered two cases corresponding to (relatively) efficient and inefficient flux transports. In the former, the relative importance of the magnetic field to the gas pressure may be kept, which then leads to a constant $\overline{\alpha_{\phi z}}$. This corresponds to our fiducial case. In the latter, the surface density decreases without varying the magnetic flux. The magnetic field strength and $\overline{\alpha_{\phi z}}$ become larger as the surface density decreases. We also consider the latter case in Section 3.2.3.

According to [M21](#) (see their Appendix B), ϵ_{rad}^1 depends mainly on the polarity of the magnetic field with ranges of $\approx 10^{-2}$ – 10^0 and $\approx 10^{-3}$ – 10^{-1} for the aligned and anti-aligned magnetic fields to the rotation axis, respectively. In this study, we adopt 0.1 as a fiducial value, which is in the range of ϵ_{rad} above. We investigate the impact of varying ϵ_{rad} in Section 3.2.1. We also set $C_{w,0}$ to be 10^{-5} , following [Suzuki et al. \(2016\)](#).

For the dust parameters, we adopt a dust-to-gas ratio f_{dg} of 0.01 and a reference opacity κ_0 of $5 \text{ cm}^2 \text{ g}^{-1}$. In Section 3.2.2, we also examine a dust model motivated by [Kondo et al. \(2023\)](#), where the dust-to-gas ratio is reduced to 0.001 while keeping the opacity unchanged.

3. Results

We first show the simulation results of the fiducial parameter set (Section 3.1) and then the dependence of the model parameters (Section 3.2). In addition, we demonstrate how the temperature model impacts planet formation (Section 3.3).

3.1. Fiducial model

Here, we present our fiducial model (**Fid**) while comparing it with a previous model (**Vis**). **Fid** is designed for wind-driven accretion disks with MHD heating: the lower heat conversion fraction is $\epsilon_{\text{rad}} = 0.1$, with surface heating where $\Sigma_{\text{heat}} = \Sigma_{\text{Am}}$. **Vis** is with classical heating: the higher conversion fraction is $\epsilon_{\text{rad}} = 0.9$ with midplane heating, $\Sigma_{\text{heat}} = \Sigma/2$. Note that in both models, accretion is mainly driven by wind stress.

To see the basic evolution of the profiles, we show the evolution of the surface density profile in the top panel of Figure 2. The basic evolution in **Fid** is consistent with that in **Vis**, which is similar to [Kunitomo et al. \(2020\)](#). The surface density decreases with time as a result of disk accretion and mass loss. Although the initial surface density profile is given by a radial power of r^{-1} for the inner region, within the first few hundred years, the surface density becomes shallower. We have confirmed that in the quasi-steady state, the net mass gains by the disk accretion and mass loss by the disk wind are almost balanced. At $t \approx 5 \text{ Myr}$, disk dissipation begins immediately from the inner region because of photoevaporation. The disk lifetime is consistent with observational suggestions (~ 3 – 10 Myr ; e.g., [Williams & Cieza 2011](#)). Note that although the overall disk evolution is similar to that of **Vis**, the surface density profile within 10 au is affected by the difference in the sound speed caused by temperature variations.

The midplane temperature also evolves with time, as shown in the lower panels of Figure 2. For **Fid**, the evolution of the

temperature profile is driven mainly by stellar luminosity evolution because irradiation heating mainly dominates the midplane temperature, as shown in detail below. Indeed, the slope is nearly constant except during the early stages of disk evolution ($\lesssim 0.1 \text{ Myr}$) and is $r^{-3/7}$. When the surface density in the inner region is quickly dropped by the photoevaporation, the stellar direct irradiation becomes able to reach the cavity after $\sim 5 \text{ Myr}$. That is why the temperature suddenly increases and makes a temperature transition at the cavity edge.

We see that the model **Fid** shows cooler disk temperatures than in **Vis**. That is also shown in the space–time temperature distribution (the upper panels of Figure 3). In the model **Fid**, the iso-temperature contours at the level larger than 100 K are located at more inner radii. This is the case also for the snowline at which $T_{\text{mid}} = 170 \text{ K}$. The snowline in the model **Fid** reaches 1 au at 0.2 Myr, while that in **Vis** reaches 1 au at 4 Myr. The early arrival of the snowline is consistent with [M21](#).

Next, we show where and when accretion heating is dominant. We calculate the ratio $(T_{\text{acc}}/T_{\text{irr}})^4$, which represents the contribution to the midplane temperature, since $T_{\text{mid}} = T_{\text{irr}}(1 + (T_{\text{acc}}/T_{\text{irr}})^4)^{1/4}$ (Equation (4)). In particular, the region where the quantity is larger than unity is the accretion-heated region. Figure 3 shows $(T_{\text{acc}}/T_{\text{irr}})^4$ in the space–time diagram. The accretion-heated region in the model **Fid** is observed only inside 0.1 au, whereas the region is very wide (within 10 au) in the model **Vis**. Even at $r \approx 0.3 \text{ au}$, as $(T_{\text{acc}}/T_{\text{irr}})^4 \approx 0.1$, the deviation from the irradiation temperature is only about 3%. Therefore, we expect that the accretion heating would operate in the limited inner region throughout the disk evolution.

To understand why accretion heating becomes subdominant, we begin by analyzing Σ_{heat} . We plot the distribution of the heating altitude z_{heat} and Σ_{heat} at various times in Figure 4. As shown in the right panel, Σ_{heat} in **Vis** is $\Sigma/2$, making Σ_{heat} usually higher than 10 g cm^{-2} . In contrast, Σ_{heat} in **Fid**, which is Σ_{Am} , remains $\lesssim 1 \text{ g cm}^{-2}$, at which the heating altitude is ~ 2 – $3 H$. Thus, the difference in Σ_{heat} can be two orders of magnitude. In addition, ϵ_{rad} differs by a factor of nine. These differences significantly suppress the temperature due to accretion heating, as in [M21](#).

Furthermore, because we consider herein the influence of mass loss on the accretion rate, we analyze the accretion rate distribution. The accretion rates induced by $r\phi$ - (e.g., viscous accretion) and ϕz -components (wind-driven accretion) stresses are given by

$$\dot{M}_{\text{acc},r\phi} = \frac{4\pi}{r\Omega} \frac{\partial}{\partial r} (r^2 \Sigma \overline{\alpha_{r\phi}} c_s^2), \quad (17)$$

$$\dot{M}_{\text{acc},\phi z} = \frac{4\pi}{\Omega} r \overline{\alpha_{\phi z}} (\rho c_s^2)_{\text{mid}}, \quad (18)$$

respectively (see [Suzuki et al. 2016](#)). We also plot the cumulative mass loss rate, which is defined as

$$\dot{M}_{\text{loss}}(r) = 2\pi \int_r^{r_{\text{out}}} r (\dot{\Sigma}_{\text{MDW}} + \dot{\Sigma}_{\text{PEW}}) dr. \quad (19)$$

The top left panel of Figure 5 shows the radial distribution ($t = 1 \text{ Myr}$) of the accretion rate in **Fid**. We see that the accretion is driven by wind stress (i.e., $\dot{M}_{\text{acc}} \approx \dot{M}_{\text{acc},\phi z}$) as the viscous accretion rate is much smaller than \dot{M}_{acc} . We find that \dot{M}_{acc} decreases from 10 au inward. At $t = 1 \text{ Myr}$, the accretion rate at $r = r_{\text{in}}$ is $3 \times 10^{-9} M_{\odot}/\text{yr}$, while the accretion rate at 10 au is $4 \times 10^{-8} M_{\odot}/\text{yr}$. The difference is due to the wind mass loss inside 1 au: 70% of the mass loss rate over the whole disk region is responsible for that within 1 au. In contrast, **Vis** shows a weaker mass loss and higher accretion rates. This is because the mass

¹ [M21](#) used $f_{\text{heat}} \equiv F_{\text{rad}}/\Gamma_{\phi z}$ instead of ϵ_{rad} . Nevertheless, in their case of $\overline{\alpha_{\phi z}} \gtrsim \overline{\alpha_{r\phi}}$, f_{heat} takes almost the same value.

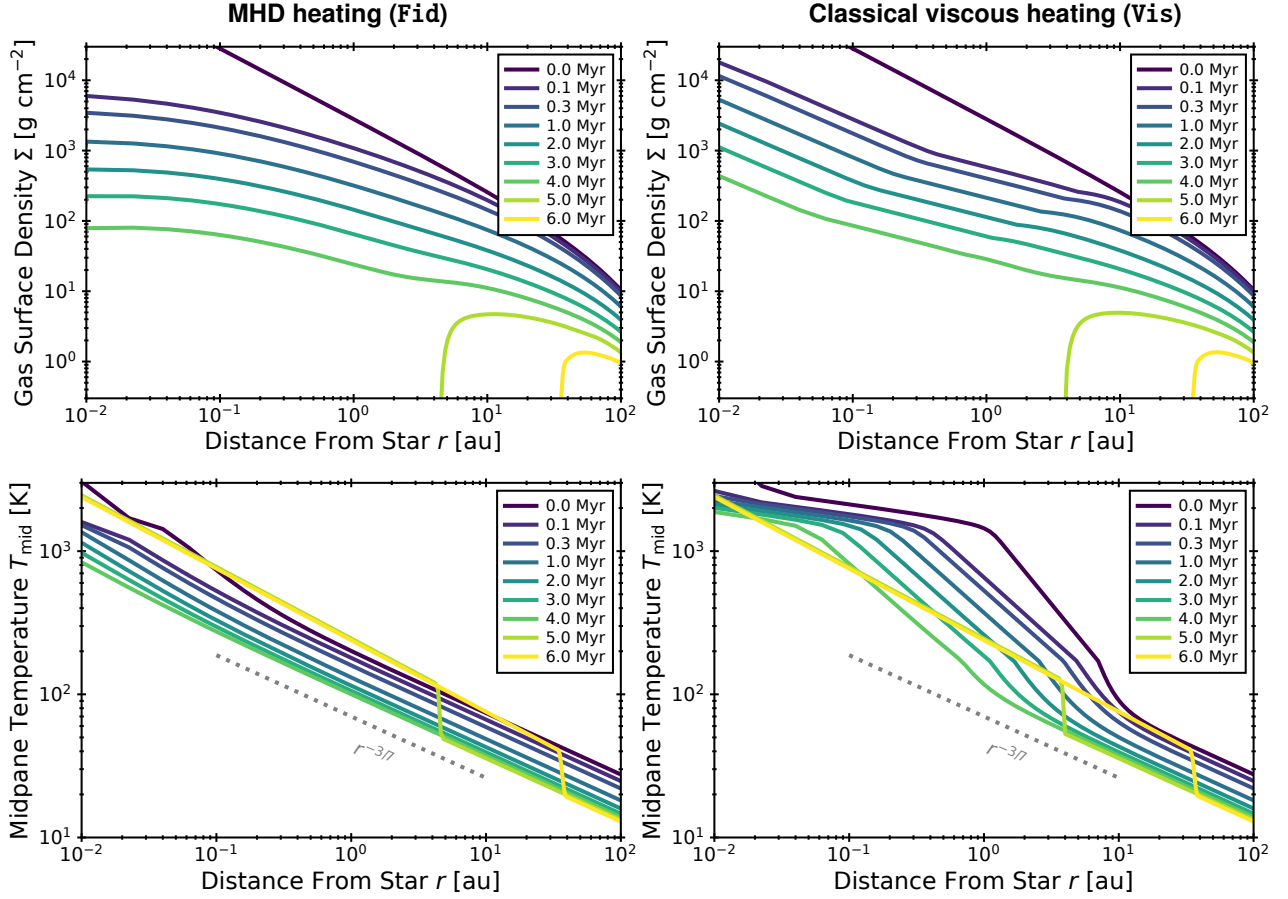


Fig. 2. Various snapshots of the radial profiles of the gas surface density (*top*) and midplane temperature (*bottom*) for the models Fid (*left*) and Vis (*right*).

loss parameter C_w is constrained by $C_{w,e}$ because of the higher ϵ_{rad} (see Section 2.3). In other words, the accretion rate is influenced by the heat production efficiency in the disks.

The lower left panel of Figure 5 shows the time evolution of the accretion rate at r_{in} and at 1 au over the disk lifetime. The difference in the accretion rates is almost one order of magnitude until disk dissipation. This clearly illustrates that wind mass loss reduces the accretion rate in the inner region.

From another perspective, this effect suggests that disk models based on the observed stellar accretion rate may underestimate the actual accretion heating within the disk. However, because of the energy removal by the disk winds and the inefficiency of surface heating, the influence of accretion heating is still considered negligible.

3.2. Parameter dependence

3.2.1. Influence of ϵ_{rad}

Although our model depends on ϵ_{rad} , the representative value is uncertain. This parameter represents the fraction of accretion energy consumed in the disk. Thus, it would depend on the details of the energy dissipation process. The local MHD simulations in M21 show that ϵ_{rad} varies between 0.5 and 5×10^{-4} . In particular, ϵ_{rad} depends on the direction of the global magnetic field penetrating the disk. The parameter ϵ_{rad} not only controls the temperature distribution but can also affect the mass loss rate and disk evolution. Here, we vary ϵ_{rad} to $\epsilon_{\text{rad}} = 1$ and $\epsilon_{\text{rad}} = 0.01$ and investigate their influence on the disk evolution.

Figure 6 shows the evolution of the accretion and mass-loss rates. When $\epsilon_{\text{rad}} = 1$, all the accretion energy is dissipated in the disk; thus, the mass loss due to the MHD disk wind does not occur (see Equation (14)). Thus, the accretion rate is uniform within 10 au. This case corresponds to the assumption in M21, where $\epsilon_{\text{rad}} = 1$ and the mass loss is negligible. For smaller ϵ_{rad} , the accretion rate decreases as in Fid, but its distribution does not vary even though ϵ_{rad} is smaller than that in Fid. This is because the mass loss rate is not affected by the change in ϵ_{rad} when $C_{w,e}$ is larger than $C_{w,0}$ in our model.

The space-time diagrams of the accretion-heated region are shown in Figure 7. For the case of $\epsilon_{\text{rad}} = 1$, the contribution of accretion heating to the midplane temperature is higher than in Fid because the energy removed by the wind is used in heating. Nevertheless, even in this extreme case, the accretion heating is weaker than that in the classical case (Vis; see Figure 7). For smaller ϵ_{rad} , by further reducing the heating energy from Fid, the accretion heating becomes subdominant even within 0.01 au.

3.2.2. Influences of dust growth

Next, we investigate the influence of the dust model on the disk structures. The temperature structure in the MHD model depends on the distribution of the opacity and ionization fraction, which are determined by dust properties (e.g., size distribution). As shown in Kondo et al. (2023), the dust growth varies both the ionization fraction and opacity, thereby affecting the strength of the accretion heating. Our model has two parameters on dust properties: dust abundance, which controls the ionization frac-

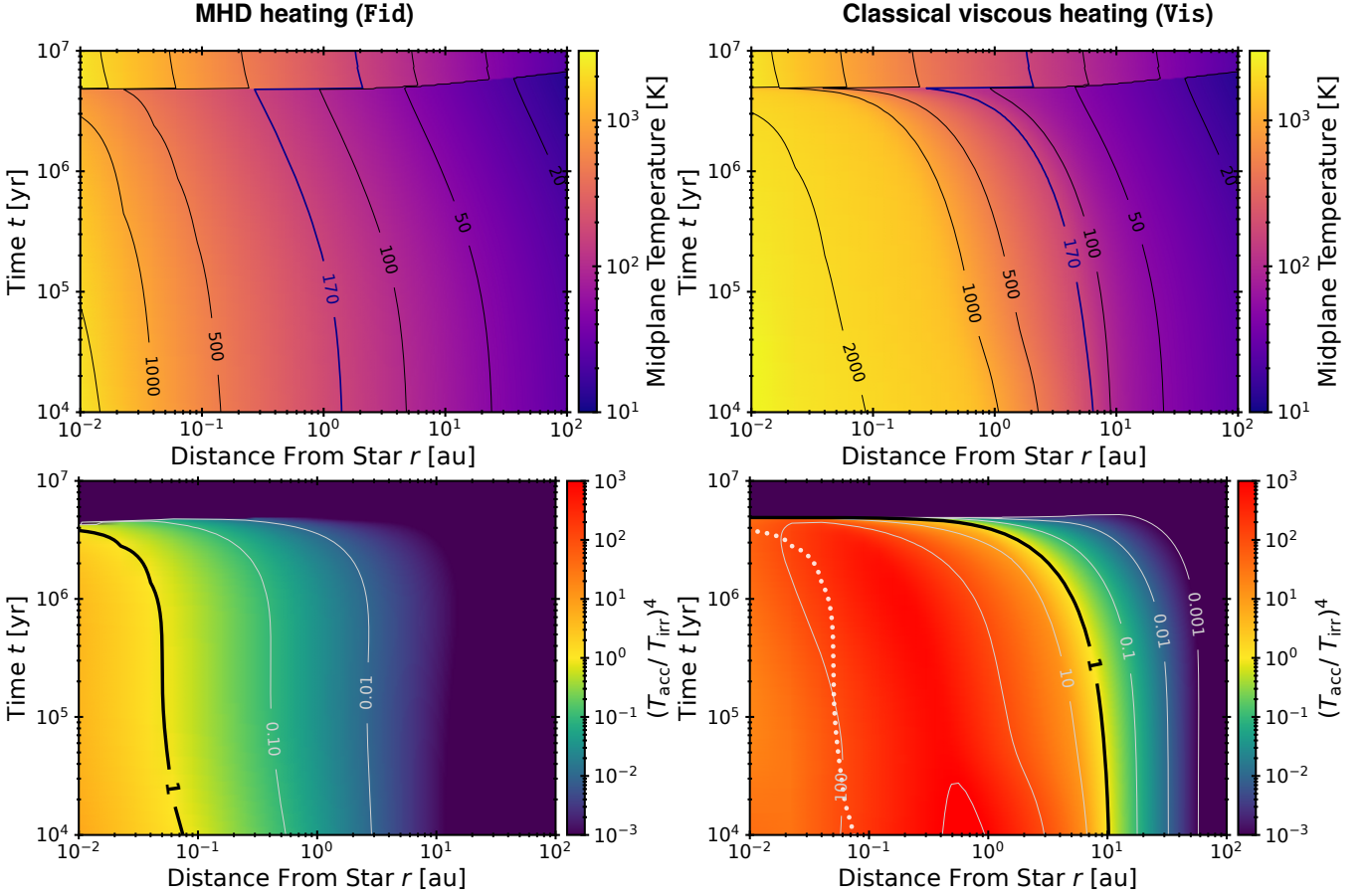


Fig. 3. *Top:* Space–time distribution of the midplane temperature. The location of the snowline ($T_{\text{mid}} = 170\text{K}$) is denoted by the thicker solid line. *Bottom:* Space–time distribution of the fourth power of the temperature ratio $(T_{\text{acc}}/T_{\text{irr}})^4$ between accretion heating and irradiation heating, indicating the contribution of accretion heating to the disk temperature. The white dotted line shows the boundary of the accretion-heated region (i.e., $(T_{\text{acc}}/T_{\text{irr}})^4 = 1$) in Fid for reference.

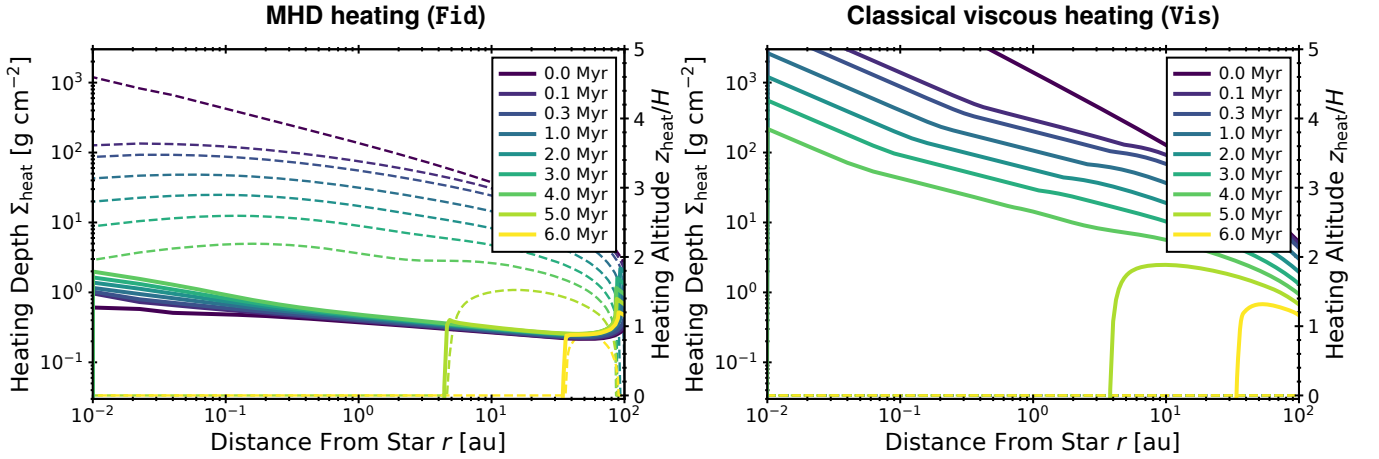


Fig. 4. Radial profiles of the heating altitude z_{heat} (dashed; right y-axis) and the column density at that altitude, Σ_{heat} (solid; left y-axis), at various times for the models Fid (left panel) and Vis (right panel). Note that we set Σ_{heat} to zero when Σ is zero.

tion, and infrared opacity, which controls the accretion heating temperature (see Section 2.2.1). Our fiducial model uses the same dust model as in M21, where the abundance and size of dust grains are like those of interstellar dust. Here, we give another dust model based on the results where the maximum size is $100\ \mu\text{m}$ in Kondo et al. (2023). This case corresponds to that where accretion heating is maximized by dust growth. To model their results, we choose the dust abundance of 10^{-3} by fixing the

total surface area with their calculation and the reference opacity of $5\text{ cm}^2\text{ g}^{-1}$.

Figure 8 shows the space–time distribution of T_{mid} and $(T_{\text{acc}}/T_{\text{irr}})^4$. In this model, the accretion-heated region extends within $\sim 0.3\text{ au}$, which is larger than that in Fid. However, the evolution of the snowline remains almost unchanged, although Kondo et al. (2023) showed that snowline migration could be delayed by dust growth. This is because in this model, ϵ_{rad} is set to a lower value of 0.1; thus, accretion heating is sufficiently

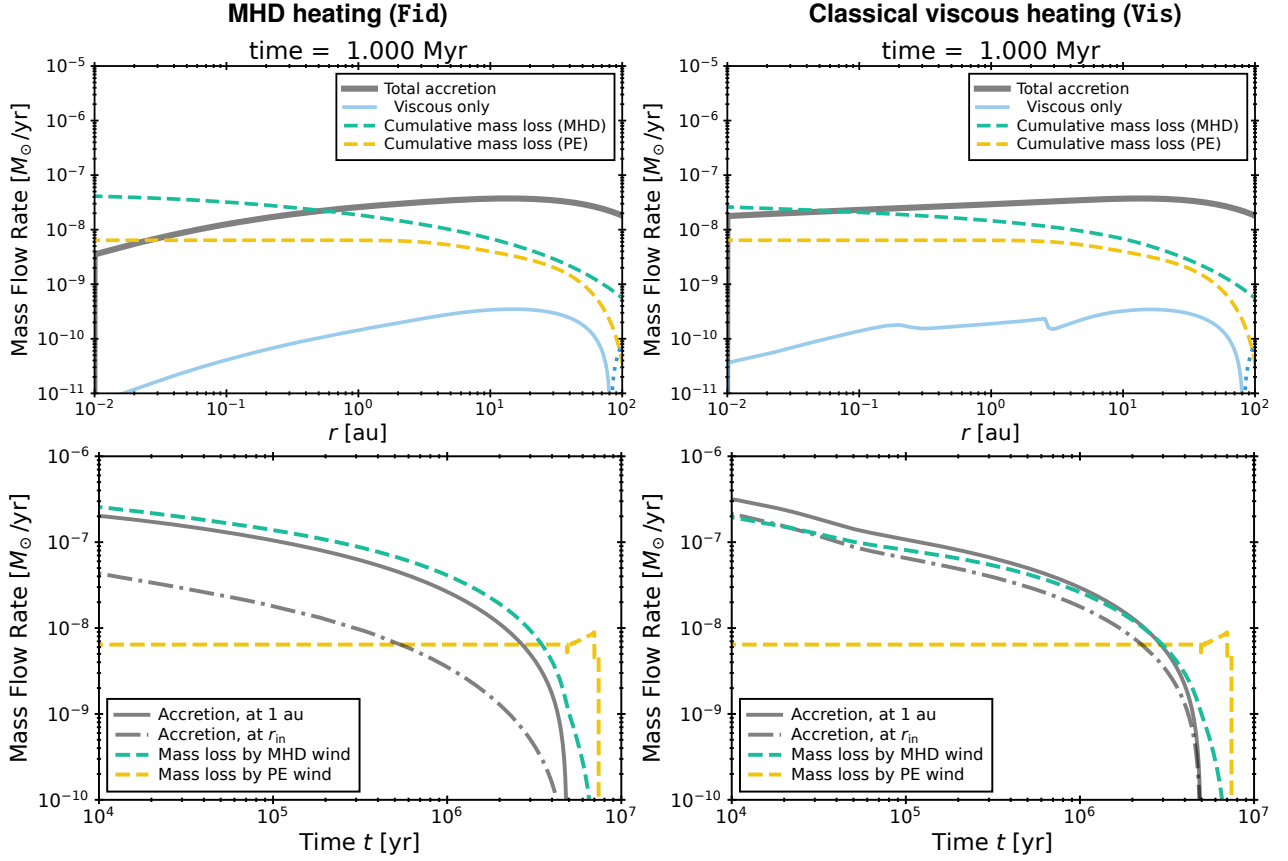


Fig. 5. *Top:* Radial profiles of the accretion rate (gray) and the cumulative mass loss rate due to MHD (green dashed) and photoevaporative winds (yellow dashed), at $t = 1$ Myr after disk formation. The accretion rate solely due to viscous stress is indicated by blue lines. The model Fid is shown in the left panels, while Vis is shown in the right panels. *Bottom:* Time evolutions of the accretion rate measured at $r = r_{\text{in}}$ ($= 0.01$ au; gray solid) and $r = 1$ au (gray dashed). The total mass loss rates by the MHD (green dashed lines) and photoevaporative winds (yellow solid) are also shown.

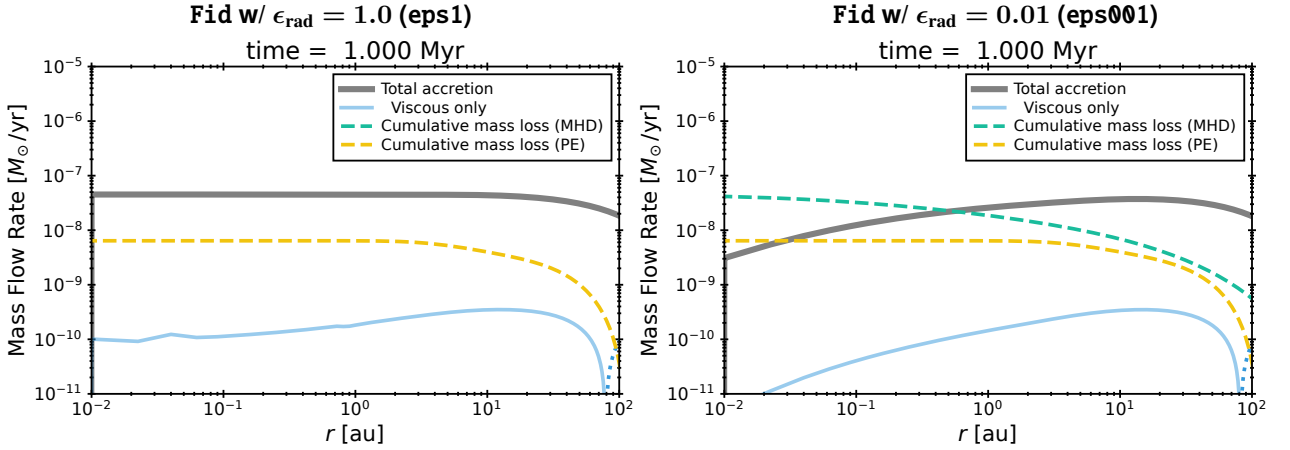


Fig. 6. Distribution of the mass accretion and loss rates as in Figure 5 but for $\epsilon_{\text{rad}} = 1$ (eps1; left) and $\epsilon_{\text{rad}} = 0.01$ (eps001; right).

weakened (see Section 4.3). This suggests that although accretion heating may be enhanced by dust growth, this effect depends on the value of ϵ_{rad} .

3.2.3. Effects of magnetic flux transport

We examine how magnetic flux transport affects the disk structure by considering the case where the magnetic stress depends on the gas surface density Σ . The time evolution and profile of $\bar{\alpha}_{\phi z}$ are sensitive to how magnetic flux is transported during disk

evolution. If the magnetic flux is transported along with the gas accretion, the relative importance of the magnetic field can be kept to some extent (Lubow et al. 1994; Okuzumi et al. 2014). Despite uncertainties in the flux transport, we assume $\bar{\alpha}_{\phi z}$ to be constant in the fiducial model (see Section 2.4). If the magnetic flux is not transported, the magnetic flux relative to the surface density is increased by the decrease in the surface density (e.g., Bai 2013). This enhances the magnetic stress. This Σ -dependent $\bar{\alpha}_{\phi z}$ model, based on the local MHD simulations (Bai 2013), is described in Suzuki et al. (2016). Here, we adopt the $\bar{\alpha}_{\phi z}$ model:

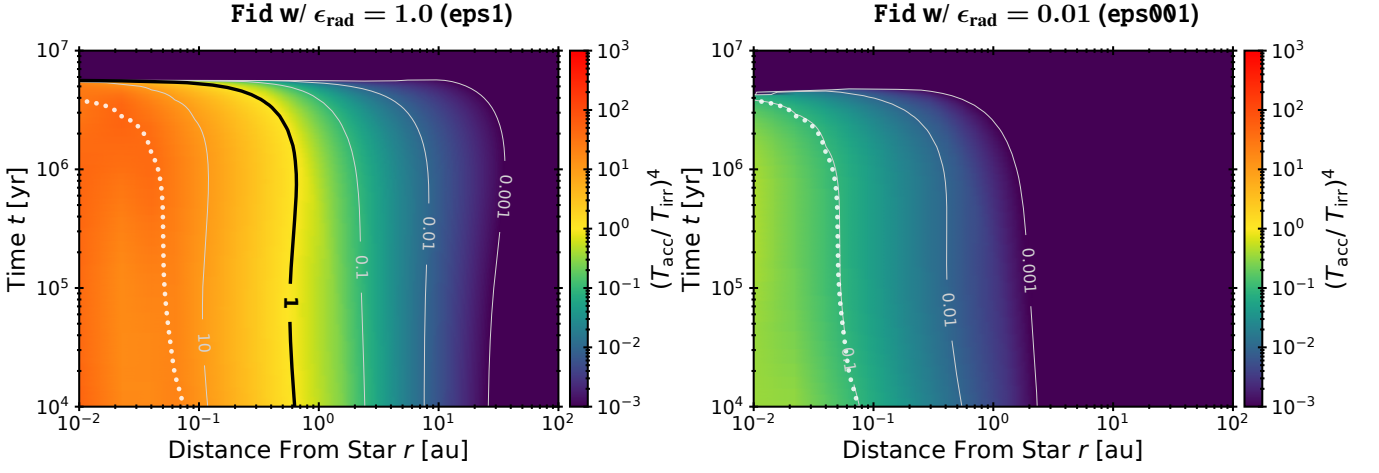


Fig. 7. Space–time distribution of $(T_{\text{acc}}/T_{\text{irr}})^4$ as in Figure 3 but for $\epsilon_{\text{rad}} = 1$ (eps1; *left*) and $\epsilon_{\text{rad}} = 0.01$ (eps001; *right*).

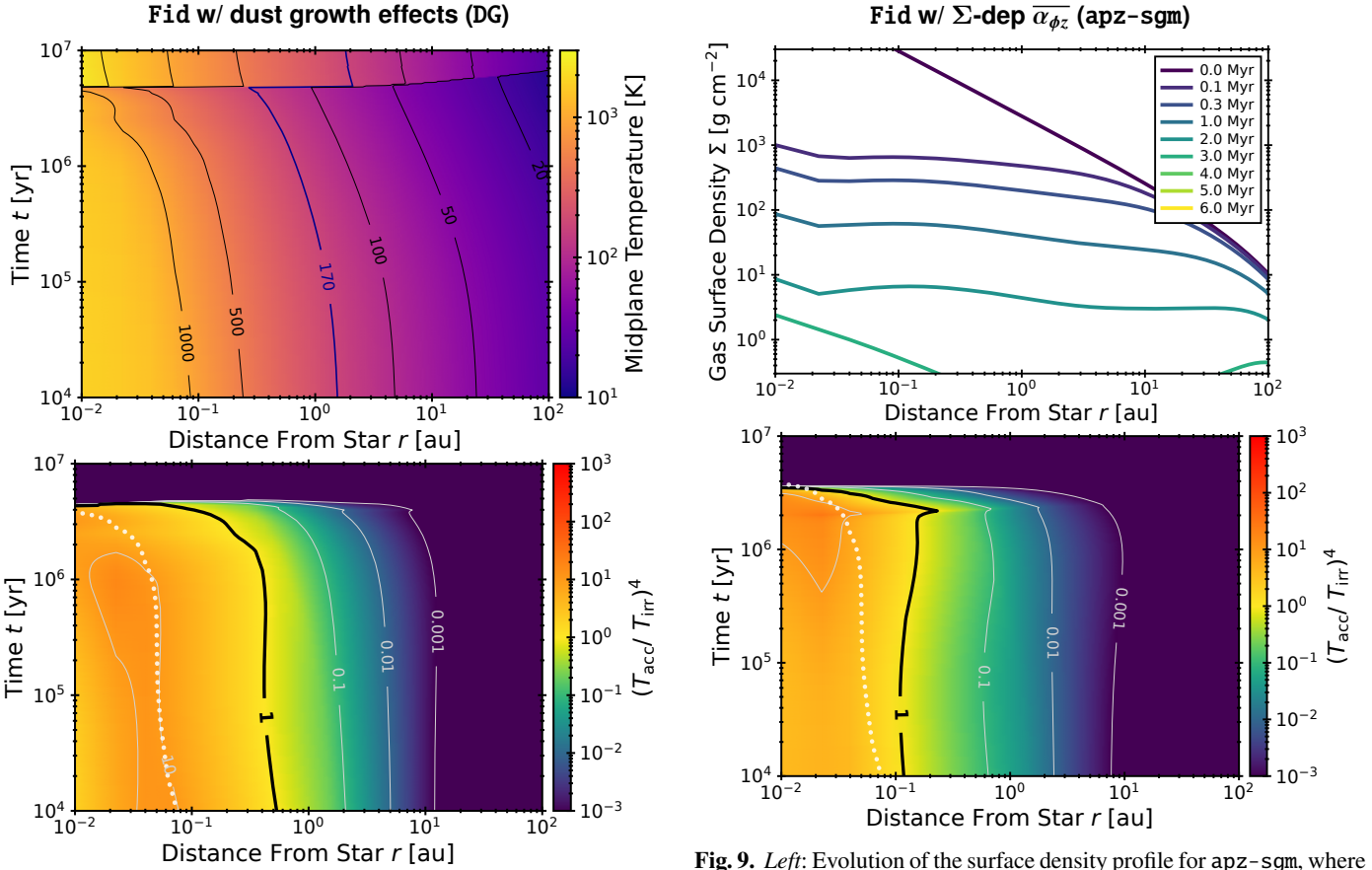


Fig. 8. Space–time distribution of T_{mid} (*top*) and $(T_{\text{acc}}/T_{\text{irr}})^4$ (*bottom*) for DG, which considers the effects of dust growth.

Fig. 9. *Left:* Evolution of the surface density profile for apz-sgm, where $\overline{\alpha_{\phi z}}$ depends on Σ . *Right:* Space–time distribution of $(T_{\text{acc}}/T_{\text{irr}})^4$ as in Figure 3 but for apz-sgm.

$$\overline{\alpha_{\phi z}} = \min \left(10^{-3} \left(\frac{\Sigma}{\Sigma_{\text{ini}}} \right)^{-0.66}, 1 \right) \quad (20)$$

where $\overline{\alpha_{\phi z}}$ increases as Σ decreases.

Figure 9 shows the evolution of Σ . In the first 0.1 Myr, the surface density rapidly decreases because the disk accretion due to $\overline{\alpha_{\phi z}}$ strengthens over time. When the accretion rate is higher than the photoevaporative mass-loss rate, gas accretion from the outer region fills the gap and maintains the surface density to

some extent (Kunitomo et al. 2020). This explains why the surface density evolution is more gradual in the late stage than in Fid.

Figure 9 also shows the space–time distribution of $(T_{\text{acc}}/T_{\text{irr}})^4$. The accretion-heated region lies within ≈ 0.1 au. Thus, even with the change in the $\overline{\alpha_{\phi z}}$ evolution, our conclusion that accretion heating is not the dominant heating source in disk evolution remains robust.

One may notice that the accretion-heated region gradually shifts outward, reaching its peak around $t = 2$ Myr. This occurs because the heating altitude approaches the midplane as Σ

decreases because of gas accretion. In previous cases, this behavior has not been observed because Σ rapidly drops because of photoevaporation.

3.3. Influences on planet formation

Here, we demonstrate the influence of the disk temperature model on planet formation processes by comparing typical cases of MHD heating (Fid) and conventional heating (Vis). We calculate the mass-orbital track for protoplanets using time-dependent disk structures obtained in calculations. We consider protoplanet growth through pebble accretion and gas accretion and migration through gravitational interaction (i.e., Types I and II migrations) with the disk gas, as described in detail in the following. Furthermore, considering the evolution of the water fraction, we address the origin of an observed dichotomy (e.g., [Parc et al. 2024](#)) in the water fraction of close-in planets in the mass range of 1–10 M_\oplus (i.e., super-Earths and sub-Neptunes).

3.3.1. Model: Growth rate and migration rate

For pebble accretion, we follow the model described in [Liu et al. \(2019\)](#) and [Ormel & Liu \(2018\)](#). The pebble accretion rate \dot{M}_{PA} is given as follows:

$$\dot{M}_{\text{PA}} = \begin{cases} (\varepsilon_{2\text{D}}^{-2} + \varepsilon_{3\text{D}}^{-2})^{-0.5} \dot{M}_{\text{peb}} & (M_p < M_{\text{iso}}) \\ 0 & (M_p \geq M_{\text{iso}}) \end{cases}, \quad (21)$$

$$\varepsilon_{2\text{D}} = \frac{0.32}{|u_{\text{dust}}|/(2v_K \text{St})} \sqrt{\frac{q_p \Delta v}{\text{St} v_K}}, \quad (22)$$

$$\varepsilon_{3\text{D}} = \frac{0.39 q_p \sqrt{1 + \text{St}/\alpha_t}}{h |u_{\text{dust}}|/(2v_K \text{St})}, \quad (23)$$

$$\Delta v = (1 + 5.7 q_p \text{St} \eta^{-3})^{-1} \eta v_K + 0.52 (q_p \text{St})^{1/3} v_K, \quad (24)$$

where M_p is the protoplanet mass, M_{iso} is the pebble isolation mass, \dot{M}_{peb} is the pebble mass flux in the disk, $q_p = M_p/M_\star$, $h = H/r$, $u_{\text{dust}} = -2\eta v_K \text{St} + v_{\text{gas}}$ with v_{gas} being the radial gas velocity, the pebble Stokes number $\text{St} \lesssim 1$, and we assume turbulence with the strength α_t controlling dust diffusion. We here take into account the gas accretion velocity in the drift speed of dust relative to protoplanets, as in [Liu et al. \(2019\)](#). The radial gas velocity v_{gas} is assumed to $-\dot{M}_{\text{acc}}/(2\pi r \Sigma)$, although it can be reduced for an efficient surface accretion ([Okuzumi 2025](#)).

To provide St , we take approach with parameterization of the pebble flux \dot{M}_{peb} , where the pebble flux parameter $\xi \equiv \dot{M}_{\text{peb}}/\dot{M}_{\text{acc}}$ as in [Ida et al. \(2016\)](#) and,

$$\xi = \begin{cases} \xi_0 & (T < 170 \text{ K}) \\ \xi_0/2 & (1500 \text{ K} > T > 170 \text{ K}) \\ 0 & (T > 1500 \text{ K}) \end{cases}, \quad (25)$$

where the ice and silicate sublimation are modeled. The reference pebble flux parameter ξ_0 is given from fitting to the result of a dust transfer simulation in Appendix A ([Birnstiel et al. 2012](#)):

$$\xi_0 = 0.15 \exp[-(t/0.05 \text{ Myr})^{0.52}]. \quad (26)$$

The pebble distributions are assumed to be in a steady state without growth calculations. The Stokes number is given by size limits of dust growth, radial drift, turbulence-induced fragmentation and drift-induced fragmentation, based on [Drażkowska et al.](#)

(2021), while we slightly update the drift limit to be applicable for small St (see Appendix B).

$$\text{St} = \min(\text{St}_{\text{drift}}, \text{St}_{\text{frag}}, \text{St}_{\text{df}}, \text{St}_{\text{growth}}) \quad (27)$$

$$\text{St}_{\text{drift}} = \frac{v_{\text{gas}}}{4\eta v_K} + \sqrt{\left(\frac{v_{\text{gas}}}{4\eta v_K}\right)^2 + 0.55 \frac{\dot{M}_{\text{peb}}}{8\pi \Sigma_g r v_K \eta |\eta|}}, \quad (28)$$

$$\text{St}_{\text{frag}} = 0.37 v_{\text{frag}}^2 / (3\alpha_t c_s^2), \quad (29)$$

$$\text{St}_{\text{df}} = v_{\text{frag}} / (|\eta| v_K), \quad (30)$$

$$\text{St}_{\text{growth}} = \frac{\pi \rho_s a_0}{2\Sigma} \exp(t\Omega\epsilon_0), \quad (31)$$

where the monomer size a_0 is set to $0.1 \mu\text{m}$, the grain internal density ρ_s is set to 1.3 g cm^{-3} , the initial dust-to-gas mass ratio ϵ_0 is set to 0.01, and we adopt fitting parameters of a dust coagulation simulation ([Birnstiel et al. 2012](#)). The fragmentation velocity v_{frag} is set to 10 m s^{-1} for fiducial case, while the case with $v_{\text{frag}} = 1 \text{ m s}^{-1}$ is shown in Appendix C. We also confirm that pebble profiles precisely match with the result of a two-population dust transport simulation ([Birnstiel et al. 2012](#)) under a given pebble flux (Appendix B).

Pebble accretion halts when a protoplanet reaches the pebble isolation mass M_{iso} ([Bitsch et al. 2018](#); [Pichierri et al. 2024](#)):

$$M_{\text{iso}} = 25 M_\oplus \left(\frac{h}{0.05} \right)^3 \left[0.34 \left(\frac{-3}{\log(\alpha)} \right)^4 + 0.66 \right] \left(\frac{3.5 + \chi}{6} \right). \quad (32)$$

Note that the original formula is based on viscous disks. Here, we simply assume α to be $\alpha_t = 10^{-4}$ because the proper treatment for α in laminar magnetized disks is unclear. We note that the pebble-isolation mass is proportional to H^3 ([Bitsch et al. 2018](#)). As shown by [Bitsch \(2019\)](#), colder disks show lower M_{iso} , whereas hotter disks show higher M_{iso} , which impacts planetary formation processes.

For a protoplanet's growth rate via gas accretion, we follow [Johansen et al. \(2019\)](#) ([Ikoma et al. 2000](#); [Tanigawa & Tanaka 2016](#))

$$\dot{M}_{\text{gas}} = \min(\dot{M}_{\text{KH}}, \dot{M}_{\text{disk}}, \dot{M}_{\text{acc}}), \quad (33)$$

$$\dot{M}_{\text{KH}} = 10^{-5} M_\oplus \text{yr}^{-1} \left(\frac{M_p}{10 M_\oplus} \right)^4 \left(\frac{\kappa_{\text{pl}}}{1 \text{ cm}^2 \text{ g}^{-1}} \right)^{-1}, \quad (34)$$

$$\dot{M}_{\text{disk}} = 0.29 h^{-2} M_p^{4/3} \Sigma r^2 \Omega \left[1 + (M_p/M_{\text{gap}})^2 \right]^{-1}, \quad (35)$$

where the opacity in the envelope of the protoplanet, κ_{pl} , is set to $1 \text{ cm}^2 \text{ g}^{-1}$, and M_{gap} is the planetary mass at which the gap opens in the disk. By increasing the protoplanet mass, the protoplanet begins to scatter the disk gas away, and the gap opens in the disk. As discussed in [Johansen et al. \(2019\)](#), the gap in the disk should be opened after the protoplanet arrives at the pebble isolation mass. Here, we also simply adopt their prescription for the gap opening mass, i.e., $M_{\text{gap}} = 2.3 M_{\text{iso}}$. Note that although this gap depth function differs slightly from those in studies modeling gap opening ([Kanagawa et al. 2018](#); [Pichierri et al. 2023, 2024](#)) and may influence planetary evolution, we confirm that it does not qualitatively affect our conclusions.

To obtain the orbital migration rate of protoplanets, we calculate formulae of planetary torque Γ given by ([Paardekooper et al. 2011](#)), which considers viscosity and thermal diffusion to retain corotation torque. For given Γ , the orbital migration rate is calculated by,

$$\dot{r}_{\text{mig}} = 2 \frac{\Gamma}{M_p r \Omega} \left[1 + (M_p/M_{\text{gap}})^2 \right]^{-1}, \quad (36)$$

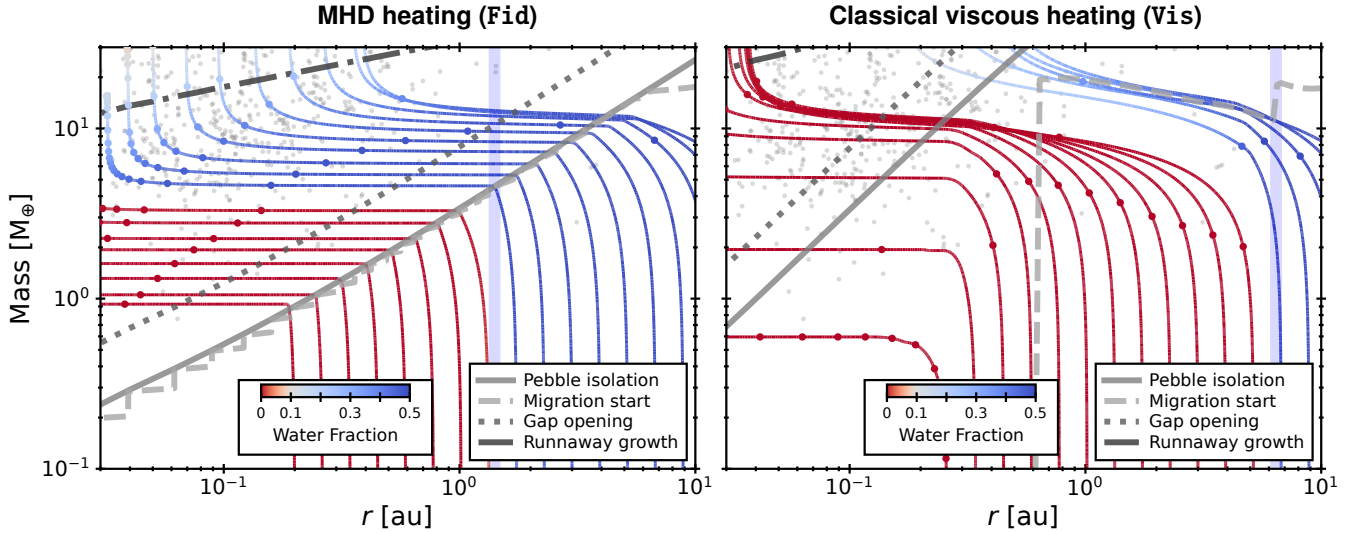


Fig. 10. Mass–orbital tracks of protoplanets starting at $M_p = 0.01 M_\oplus$ and $r = [0.2:20]$ au, with early-onset growth ($t_0 = 0.01$ Myr) and $v_{\text{frag}} = 10 \text{ m s}^{-1}$, under MHD heating (left) and classical heating (right). The total pebble mass drifting through the snowline at $t \geq t_0$ is $400 M_\oplus$. Characteristic masses in planetary evolution at $t = 0.1$ Myr are also shown as gray lines. Planets grow through pebble accretion until they reach the isolation mass (M_{iso} ; solid line). When the growth timescale exceeds the migration timescale, migration becomes the dominant process (M_{mig} ; dashed line). Gaps start to open when M_p reaches $2.3M_{\text{iso}}$ (M_{gap} ; dotted line). Planets grow in a runaway manner when the growth timescale becomes shorter than the migration timescale again (M_{RG} ; dash-dotted line). Points on each mass–orbital track show the elapsed time for every 0.5 Myr. Gray circular points show the distribution of confirmed exoplanets orbiting stars with masses in the range of $[0.8, 1.2]M_\odot$ (NASA Exoplanet Archive 2024). Vertical blue lines show the location of the snowline at $t = 0.1$ Myr.

where the factor $\left[1 + \left(M_p/M_{\text{gap}}\right)^2\right]^{-1}$ is introduced to suppress the migration rate when the gap is opened as in Johansen et al. (2019).

3.3.2. Mass-orbital track

We put protoplanets with $M_p = 0.01 M_\oplus$ at $t_0 = 0.01$ Myr (the onset time of protoplanet growth) in the disk evolution models with MHD heating (left) and classical heating (right). The obtained mass–orbital tracks are shown as lines in Figure 10. We also show the water fraction of the protoplanets. We assume that the water fraction of pebbles is 50% outside the snowline, while it is zero inside the snowline. We also assume that the water fraction of the disk gas is zero outside the snowline, while it is 0.005 inside the snowline (Lodders 2003).

To better understand the growth and migration of protoplanets, we also show characteristic masses based on the disk structures at $t = t_0$. The first one is the pebble isolation mass M_{iso} (solid line) as described in Equation (32). The second one is the migration initiation mass M_{mig} (dashed line), which is the mass at which the migration timescale (r/\dot{r}_{mig}) becomes shorter than the growth timescale (M_p/\dot{M}_{peb}). The third one is the gap opening mass M_{gap} ($= 2.3M_{\text{iso}}$; dotted line), which is the mass at which the gap opens in the disk. The last one is the runaway growth mass M_{RG} (dash-dotted line), which is the mass at which the growth timescale ($= M_p/\dot{M}_{\text{gas}}$) becomes shorter than the migration timescale again.

We begin with the case of the classical heating model (Vis). In this model, the high disk temperature leads to a large pebble isolation mass. In this parameter set for young PPDs, the protoplanets efficiently grow via pebble accretion due to the high pebble mass flux. While the migration initiation mass is higher than $10 M_\oplus$ at $t = t_0$, it decreases as the pebble flux decreases. Thus, the protoplanets begin to migrate inward around $M \sim 4\text{--}10 M_\oplus$ before reaching the pebble isolation mass. The inner protoplan-

ets do not grow until the disk temperature is enough decreased ($T < 1500 \text{ K}$).

On the other hand, the colder disk model (Fid) shows a distinct evolutionary path. The reduced aspect ratio h lowers the pebble isolation mass and increases pebble accretion efficiency due to the inverse dependence on η ($\propto h^2$). As a result, protoplanets rapidly reach the isolation mass and begin migrating inward as pebble accretion ceases. Although gap opening slows this migration (i.e., Type II migration), lower-mass protoplanets ($M_p \lesssim 4 M_\oplus$) still migrate inward on short timescales. To match the observed exoplanet distribution, additional disk structures would be required to halt or slow this migration. Meanwhile, more massive protoplanets ($M_p \sim 10 M_\oplus$) undergo runaway gas accretion and form close-in gas giants.

Differences in the disk models affect the water content of protoplanets. In model Vis, a high M_{iso} and distant snowline lead to fully rocky super-Earth/sub-Neptune protoplanets. In contrast, model Fid, with a lower M_{iso} and a closer-in snowline, shows a transition from rocky to water-rich compositions around $M_p \sim 4 M_\oplus$. This agrees with an observation indicating a compositional transition near $4.2 M_\oplus$ for FG-type stars (Parc et al. 2024). Although our parameter sets in Appendix C show varying transition masses, the presence of the transition around a few M_\oplus is less sensitive to disk parameters than in Vis. Even when the transition occurs at lower masses, collisional merging, which is neglected here, may shift the transition mass higher.

Note that even in viscous disks the observed water transition may occur if the planetary growth timescale is comparable to the inward migration timescale at $M_p \sim$ a few M_\oplus , as in previous studies (Venturini et al. 2020; Izidoro et al. 2021, 2022). For example, pebble accretion-driven migration may further enhance inward migration, potentially leading to the formation of volatile-rich sub-Neptunes (Lambrechts et al. 2019; Izidoro et al. 2021). However, recent hydrodynamical/particle simulations indicate that gravitational torques from pebbles distribution can generate positive torques on protoplanets

(Benítez-Llambay & Pessah 2018; Chrenko et al. 2024), which may suppress or even reverse the inward migration induced by pebble accretion. Alternatively, in low-mass disk scenarios the lower pebble flux and lower temperatures may lead to volatile-rich planets. Venturini et al. (2020) demonstrated that an initial disk mass of $0.03 M_{\odot}$ can produce the volatile transition at $M_p \sim 4\text{--}7 M_{\oplus}$, although the disk accretion rate might be inconsistent with observed stellar accretion rates (e.g., Testi et al. 2022, see also Section 4.2). Furthermore, as shown in Appendix C (panel (d) of Figure C.1), a case with later onset of the protoplanet growth ($t_0 = 0.2$ Myr) shows the transition in the planetary water fraction in Vis.

Note that even in viscous disks, the observed water transition may occur if the planetary growth timescale is comparable to the inward migration timescale at $M_p \sim$ a few M_{\oplus} , as in previous studies (e.g., Venturini et al. 2020; Izidoro et al. 2021, 2022). For instance, as shown in Appendix C (panel (d) of Figure C.1), a case with a later onset of protoplanet growth ($t_0 = 0.2$ Myr) shows a transition in the water fraction around $M_p \sim 4 M_{\oplus}$ even in Vis. Furthermore, as in Venturini et al. (2020), lower disk masses can lead to a modest reduction in pebble accretion efficiency. Additional migration torques, such as angular momentum changes due to pebble accretion (Lambrechts et al. 2019; Izidoro et al. 2021) and thermal torques (Guilera et al. 2019; Venturini et al. 2020), alter the migration timescale and influence the conditions under which the water fraction transition at a few M_{\oplus} occurs.

Nevertheless, it is worth emphasizing that when the pebble isolation mass is as low as in our models, efficient pebble accretion alone can account for the coexistence of rocky and volatile-rich planets for close-in planets. The early onset of protoplanet growth is also consistent with observed disk mass statistics, which suggest that planet formation likely begins early in disk evolution (e.g., Andrews 2020). Furthermore, in Appendix C, we explore the cases in which v_{frag} and t_0 are varied and find that the transition in water fraction occurs around a few Earth masses. Taking into account collisional merging may further help to reproduce the observed water-fraction transition. In contrast, for viscous disks with a higher pebble isolation mass, reproducing the water-fraction transition requires fine-tuning of model parameters.

The results also provide implications for Earth’s formation. If a protoplanet with $M_p \sim 0.01 M_{\oplus}$ exists at 1 au, it would quickly reach the pebble isolation mass higher than $1 M_{\oplus}$, even when the pebble isolation mass is small (Fid). To avoid this, the pebble flux should have been suppressed well during the Earth formation. This might be due to the halting of pebble drift by the Jupiter-created gap or the depletion of dust in the disk.

Note that the present calculation neglects planetary growth through collisions with protoplanets or planetesimals. If collisional growth is significant, protoplanets may acquire mass additionally, potentially leading to the formation of larger planetary bodies. In addition, gap formation by protoplanets in the outer region can influence the pebble flux delivered to the inner disk. Furthermore, recycling of vapor around protoplanets (Johansen et al. 2021; Wang et al. 2023; Müller et al. 2024) and heating by the ^{26}Al radionuclide in planetesimal-sized bodies (Lichtenberg et al. 2019, 2021) can suppress planetary water content, potentially facilitating the formation of rocky planets in the later phases of disk evolution. Detailed studies of planet formation within more comprehensive models are therefore required. Nonetheless, our study highlights the role of pebble accretion alone in shaping the water-fraction distribution across planetary masses.

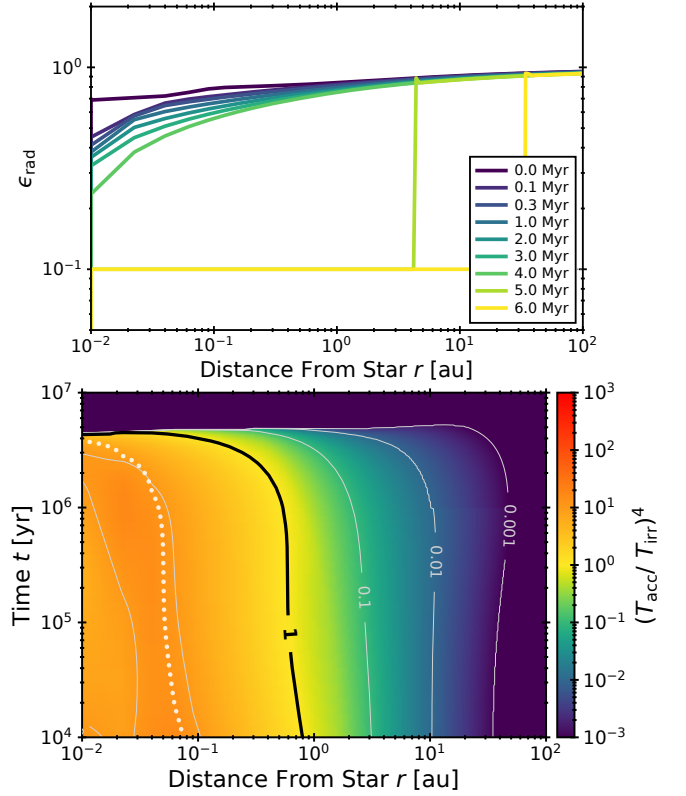


Fig. 11. Space–time distribution of ϵ_{rad} (top) and $(T_{\text{acc}}/T_{\text{irr}})^4$ (bottom) as in Fid, but modified to meet the energy balance.

4. Discussion

4.1. Influences of energetics

In this paper, the parameter $C_{w,0}$ is used to determine the mass-loss rate of MHD winds. Simultaneously, ϵ_{rad} determines the energy used for accretion heating. One may notice an imbalance between the generated and lost energies. When $C_{w,0}$ is less than $C_{w,e}$, it implies the presence of some energy in the MHD wind. However, these parameters have been obtained from different local simulations, which cannot correctly capture the wind energy in the outer limit. Therefore, the actual balance between wind energy and heating energy is still highly uncertain. As a possibility, while the wind energy (i.e., E_w) is maintained to be low or zero, the rest of the energy may be used for heating (see Equation (13)).

Here, we demonstrate how much the unused energy affects the disk temperature. At the radius where $C_{w,0} > C_{w,e}$, whereas the mass loss rate is determined by $C_{w,0}$ as in the fiducial cases (Equation (15)), ϵ_{rad} is increased so that the energy balance with the zero wind energy meets

$$F_{\text{rad}} = \Gamma_{r\phi} + \Gamma_{\phi z} - \dot{\Sigma}_{\text{MDW}} r^2 \Omega^2 / 2 \quad (37)$$

We apply this approach to Fid. Figure 11 shows the ϵ_{rad} profile and the space–time distribution of $(T_{\text{acc}}/T_{\text{irr}})^4$. We see that ϵ_{rad} deviates from 0.1 and ≈ 1 in the outer region, at $t <$ a few Myr. Since ϵ_{rad} is 0.1 in Fid, this suggests that most of the accretion energy is neglected in the outer region. However, as in Section 3.2.1, even with $\epsilon_{\text{rad}} = 1$, the efficient cooling of the surface heating results in a cooler disk temperature than in Vis.

How C_w and ϵ_{rad} should be set is still unclear, although MHD simulations have measured the mass loss rate (e.g. Suzuki & Inutsuka 2009; Lesur 2021). The value of C_w varies

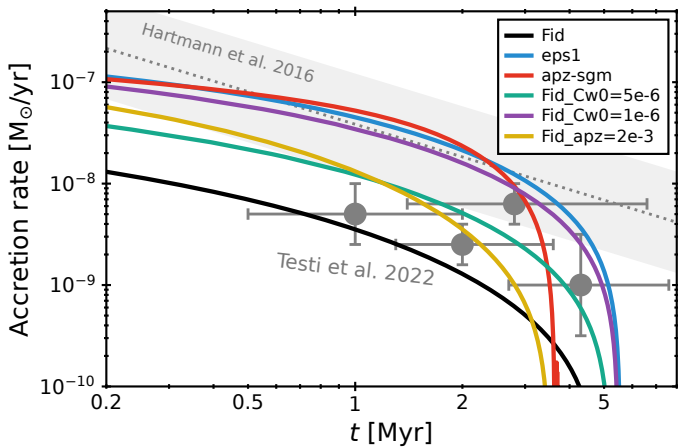


Fig. 12. Evolution of the accretion rate in our simulations (solid lines) and the observational relation between the accretion rate and stellar age. The simulated accretion rates are measured at the inner boundary of the simulation domain. The observational \dot{M} - t relations for $1 M_{\odot}$ stars derived by Hartmann et al. 2016 (gray dotted-line and shade) and Testi et al. 2022 (dark gray points with bars) are shown. The horizontal bars show the 25th to 75th percentile range of stellar ages in each star-forming region.

among different simulations; in particular, it is strongly dependent on the strength of the magnetic field (Lesur 2021). In addition, C_w obtained in simulations might be too large, resulting in inconsistencies with observations, such as the disk lifetime. The evolution of the magnetic field must be revealed to understand the disk wind strength ($\alpha_{\phi z}$ as well; Section 3.2.3). Further research is necessary to determine the appropriate combination of C_w and ϵ_{rad} that is consistent with the energy balance.

4.2. Comparison with observational \dot{M} - t relations

Here, we discuss the consistency of our accretion rate evolutions with the observed relation between the stellar accretion rate and age (e.g., Hartmann et al. 1998, 2016; Sicilia-Aguilar et al. 2010; Testi et al. 2022). Hartmann et al. (2016) presented the empirical \dot{M} - t relation² for $M \approx 1 M_{\odot}$ stars, $\dot{M} = 4 \times 10^{-8 \pm 0.5} M_{\odot}/\text{yr} (t/1 \text{ Myr})^{-1.07}$, where the mass dependence has been taken into account. Testi et al. (2022) also analyzed the accretion rate for different star-forming regions and derived the \dot{M} - t relation. Both relations are shown in Figure 12. Note that there may be a bias where stars with higher \dot{M} are easily observed. We see that the observational relation still has a scatter on the accretion rate, which may depend on the observations and analyses.

The simulated $\dot{M}(r_{\text{in}})$ evolutions are expected to intersect with the observed relation at some point if the simulation reproduces typical disk evolutions. Note that since the simulation only represents a single case, its accretion rate evolution does not need to fully follow observations. Figure 12 also shows several \dot{M} evolutions from our simulations. The stellar accretion rate in Fid deviates from Hartmann’s relation. The reduced accretion rate in Fid is caused by the mass loss by disk winds (see Figure 5). However, the accretion rate evolution in Fid is consistent with the mean values of two star-forming regions in Testi et al. (2022). Thus, Fid can explain stars with lower accretion rates.

² We note that although Hartmann et al. (2016) derived stellar ages with the original version of stellar evolutionary models by Feiden (2016), we shifted the time in our stellar luminosity evolution (see Section 2.2.2).

Even in our simulations, higher accretion rates can be obtained by adjusting the disk model parameters within their uncertainties. When ϵ_{rad} is set to unity (see the model eps1), the accretion rate exceeds that of Fid because there is no wind mass loss. The evolutionary model with a Σ -dependent $\alpha_{\phi z}$ also keeps the accretion rate higher (see the model apz-sgm). In both cases, the accretion rates are higher than in Fid, which can account for stars with higher accretion rates. In addition, we performed new simulations with parameter variations from Fid, as shown by the Fid_* models in Figure 12. The model Fid_apz=2e-3 shows that a simple doubling of $\alpha_{\phi z}$ can also lead to higher accretion rates. If we change $C_{w,0}$ to 5×10^{-6} (Fid_Cw0=5e-6) and 1×10^{-6} (Fid_Cw0=1e-6), then changing $C_{w,0}$ by an order of magnitude can account for all the median points in Testi et al. (2022). These models correspond to the case where the wind mass loss is more or less weaker than assumed in Fid. Therefore, by considering the dispersion of the wind mass loss rates for each object, we can explain the observed \dot{M} - t relation in wind-driven accretion disks.

Note that the disk winds in the inner region may fail to escape the gravitational potential and accrete to the star directly. Takasao et al. (2022) showed that after disk winds are launched from the surrounding disk to the star, they fall toward the star. This may happen for winds launched around $r \approx 0.1$ –1 au.

4.3. Updates from previous migration snowlines

Here, we describe updates on the snowline migration compared with those in previous studies. In our calculations, the migration of the snowlines basically arrives at 1 au in the early stage of the Class II disk evolution. The typical arrival time at 1 au is $t \approx 0.2$ Myr, which is earlier than that in M21. This arrival time is still the case even in DG, where accretion heating is enhanced by dust growth (Kondo et al. 2023). One update is that the ϵ_{rad} we have chosen is 10 times smaller than those of previous studies. In addition, the wind mass loss may reduce the accretion rate by a factor of ~ 2 –5. Furthermore, in our model, we modified $t = 0$ in the luminosity evolution to be on the birthline (Stahler & Palla 2004), as described in Section 2.2.2. This decreases the luminosity at $t \lesssim 0.5$ Myr, making the arrival time earlier. If such early arrivals of the snowline are the case, to avoid involving icy dust in rocky protoplanets, the formation of rocky protoplanets in Class 0–I phase may be plausible.

Moreover, in this work, by considering disk dispersal, we newly obtain the inner limit of the snowline. The limit is about 0.3 au, independent of accretion heating models. One might naively expect that if disk dispersal occurs before the snowline arrival at 1 au, the Earth would not be exposed to the icy material. However, even in the Vis model, the snowline stays within 1 au for ~ 1 Myr before disk dispersal. If disk dispersal occurs suddenly, it would have to happen earlier than 1 Myr, which conflicts with the observed disk lifetime. Thus, disk dispersal would not prevent the Earth from being exposed to icy material.

4.4. Caveats: Thermal ionization in the innermost region

In this study, thermal ionization is not taken into account, which occurs at $T \gtrsim 1000$ K (see Desch & Turner 2015). Once thermal ionization occurs, it may increase the ionization fraction and then trigger MRI. The MRI turbulence may cause viscous heating and then maintain the thermal ionization and turbulence (M21). This effect may influence the temperature structure within ~ 1 au in the early phase and within ~ 0.1 au in the late

phase, as well as the evolution of protoplanets (Section 3.3). The sustainability of this self-sustained MRI remains uncertain and needs to be investigated in future studies.

5. Summary

In this study, we investigated the evolution of the thermal structure of magnetized disks with wind mass loss. Our model is designed to be magnetized wind-driven accretion disks, where accretion is driven by wind stress. The temperature model incorporates recent findings: the surface heating and energy loss by disk wind. In addition, whereas the previous studies (M21; Kondo et al. 2023) have assumed uniform accretion rates, the accretion rate distribution is affected by the wind mass loss. This study highlighted the importance of choosing the temperature model to be consistent with disk dynamics and demonstrated that the difference in the temperature model impacts the formation of super-Earths and sub-Neptunes.

Our findings are as follows,

- *Lower temperatures in MHD disks.* The temperature profile in the MHD heating model is invariably lower than in the classical heating model, with differences reaching up to a factor of five. The main contributor to the attenuation of accretion heating is the reduced effective optical depth due to surface heating in the MHD heating. In addition, energy loss due to disk winds further reduces the accretion heating. Furthermore, even in inner regions, the accretion rate is suppressed by wind mass loss, which reduces the accretion heating.
- *Limited accretion-heated region.* The accretion-heated region is limited within 0.1–1 au, even in the early phase of Class II. This means that the overall temperature profile is primarily shaped by irradiation heating, which allows us to simplify models of the temperature structure and evolution of protoplanetary disks.
- *Impact on planetary evolution and water fraction.* Differences in temperature models significantly impact planetary evolution and water fraction. In the MHD heating model, the pebble isolation mass is smaller than in the classical heating model because of the lower temperature. In addition, as the snowline lies at inner radii in the MHD heating model, the obtained close-in planets have a dichotomy of lower-mass rocky planets and higher-mass volatile-rich planets, which transitions around $M_p \approx 4 M_\oplus$. This dichotomy appears to be consistent with exoplanet observations (e.g., Parc et al. 2024).

In the discussion, although the stellar accretion rate in our model is suppressed by wind mass loss, it may be consistent with the observational relation of the stellar accretion rate and age (see Section 4.2). Note that the observational relation still has large uncertainties.

This study encourages further investigation into the earlier phases of disk evolution (i.e., Class 0–I). Whereas the disk temperature during the Class II phase may be cold, as suggested by MHD disk models, earlier disks are likely more massive due to gas infall from the cloud core (e.g., Kimura et al. 2016; Marshall & Morbidelli 2023). This could trigger gravitational instability, leading to shock and compressional heating from gravitational spirals, which efficiently heats the disk. Future studies are needed on the evolution of temperature structures from disk formation to dispersal.

Acknowledgements. We thank Takeru Suzuki and Xuening Bai for valuable discussions, particularly regarding the energetics of our model, and Satoshi

Okuzumi for his insightful comments on the comparison with observational data. We also thank Chris Ormel, Bertram Bitsch, Alessandro Morbidelli, Tristan Guillot, and Aurélien Crida, and the anonymous referee for insightful discussions and constructive feedback. This research has made use of the NASA Exoplanet Archive, which is operated by the California Institute of Technology, under contract with the National Aeronautics and Space Administration under the Exoplanet Exploration Program. S.M. is supported by the JSPS KAKENHI (grant Nos. JP21J00086, 22KJ0155, and 22K14081) and Shuimu Tsinghua Scholar program. M.K. is supported by the JSPS KAKENHI (grant Nos. 23H01227, 24K00654, and 24K07099) and thanks Observatoire de la Côte d’Azur for the hospitality during his long-term stay in Nice. M.O. is supported by the National Natural Science Foundation of China (Nos. 12273023, 12250610186). Numerical computations were partially carried out on a PC cluster at the Center for Computational Astrophysics, National Astronomical Observatory of Japan.

References

- Affolter, L., Mordasini, C., Oza, A. V., Kubyshkina, D., & Fossati, L. 2023, *A&A*, 676, A119
- Alexander, R. D. & Armitage, P. J. 2007, *MNRAS*, 375, 500
- Alexander, R. D., Clarke, C. J., & Pringle, J. E. 2006, *MNRAS*, 369, 216
- Andrews, S. M. 2020, *ARA&A*, 58, 483
- Bai, X.-N. 2013, *ApJ*, 772, 96
- Bai, X.-N. 2016, *ApJ*, 821, 80
- Bai, X.-N. 2017, *ApJ*, 845, 75
- Bai, X.-N. & Stone, J. M. 2013, *ApJ*, 769, 76
- Bai, X.-N., Ye, J., Goodman, J., & Yuan, F. 2016, *ApJ*, 818, 152
- Balbus, S. A. & Hawley, J. F. 1991, *ApJ*, 376, 214
- Benítez-Llambay, P. & Pessah, M. E. 2018, *ApJ*, 855, L28
- Birnstiel, T., Klahr, H., & Ercolano, B. 2012, *A&A*, 539, A148
- Bitsch, B. 2019, *A&A*, 630, A51
- Bitsch, B., Lambrechts, M., & Johansen, A. 2015, *A&A*, 582, A112
- Bitsch, B., Morbidelli, A., Johansen, A., et al. 2018, *A&A*, 612, A30
- Blandford, R. D. & Payne, D. G. 1982, *MNRAS*, 199, 883
- Burn, R., Mordasini, C., Mishra, L., et al. 2024, *Nature Astronomy*, 8, 463
- Chambers, J. 2023, *ApJ*, 944, 127
- Chiang, E. I. & Goldreich, P. 1997, *ApJ*, 490, 368
- Chrenko, O., Chametla, R. O., Masset, F. S., Baruteau, C., & Brož, M. 2024, *A&A*, 690, A41
- Desch, S. J. & Turner, N. J. 2015, *ApJ*, 811, 156
- Drążkowska, J., Stammer, S. M., & Birnstiel, T. 2021, *A&A*, 647, A15
- Feiden, G. A. 2016, *A&A*, 593, A99
- Gammie, C. F. 1996, *ApJ*, 457, 355
- Ginzburg, S., Schlichting, H. E., & Sari, R. 2018, *MNRAS*, 476, 759
- Goldreich, P. & Tremaine, S. 1979, *ApJ*, 233, 857
- Gressel, O., Turner, N. J., Nelson, R. P., & McNally, C. P. 2015, *ApJ*, 801, 84
- Guilera, O. M., Cuello, N., Montesinos, M., et al. 2019, *MNRAS*, 486, 5690
- Gupta, A. & Schlichting, H. E. 2019, *MNRAS*, 487, 24
- Hartmann, L., Calvet, N., Gullbring, E., & D’Alessio, P. 1998, *ApJ*, 495, 385
- Hartmann, L., Herczeg, G., & Calvet, N. 2016, *ARA&A*, 54, 135
- Hayashi, C. 1981, *Progress of Theoretical Physics Supplement*, 70, 35
- Hayashi, C., Nakazawa, K., & Mizuno, H. 1979, *Earth and Planetary Science Letters*, 43, 22
- Hirose, S. & Turner, N. J. 2011, *ApJ*, 732, L30
- Hubeny, I. 1990, *ApJ*, 351, 632
- Ida, S., Guillot, T., & Morbidelli, A. 2016, *A&A*, 591, A72
- Ida, S., Yamamura, T., & Okuzumi, S. 2019, *A&A*, 624, A28
- Ikoma, M., Nakazawa, K., & Emori, H. 2000, *ApJ*, 537, 1013
- Iwasaki, K., Tomida, K., Takasao, S., Okuzumi, S., & Suzuki, T. K. 2024, *PASJ*, 76, 616
- Izidoro, A., Bitsch, B., Raymond, S. N., et al. 2021, *A&A*, 650, A152
- Izidoro, A., Schlichting, H. E., Isella, A., et al. 2022, *ApJ*, 939, L19
- Johansen, A., Ida, S., & Brasser, R. 2019, *A&A*, 622, A202
- Johansen, A., Ronnet, T., Bizzarro, M., et al. 2021, *Science Advances*, 7, eabc0444
- Kanagawa, K. D., Tanaka, H., & Szuszkiewicz, E. 2018, *ApJ*, 861, 140
- Kimura, S. S., Kunitomo, M., & Takahashi, S. Z. 2016, *MNRAS*, 461, 2257
- Komaki, A., Nakatani, R., & Yoshida, N. 2021, *ApJ*, 910, 51
- Kondo, K., Okuzumi, S., & Mori, S. 2023, *ApJ*, 949, 119
- Kudoh, T. & Shibata, K. 1995, *ApJ*, 452, L41
- Kunitomo, M., Ida, S., Takeuchi, T., et al. 2021, *ApJ*, 909, 109
- Kunitomo, M., Suzuki, T. K., & Inutsuka, S.-i. 2020, *MNRAS*, 492, 3849
- Kusaka, T., Nakano, T., & Hayashi, C. 1970, *Progress of Theoretical Physics*, 44, 1580
- Lambrechts, M. & Johansen, A. 2014, *A&A*, 572, A107
- Lambrechts, M., Johansen, A., & Morbidelli, A. 2014, *A&A*, 572, A35
- Lambrechts, M., Morbidelli, A., Jacobson, S. A., et al. 2019, *A&A*, 627, A83
- Lesur, G. R. J. 2021, *A&A*, 650, A35

- Lichtenberg, T., Drażkowska, J., Schönbachler, M., Golabek, G. J., & Hands, T. O. 2021, *Science*, 371, 365
- Lichtenberg, T., Golabek, G. J., Burn, R., et al. 2019, *Nature Astronomy*, 3, 307
- Lin, D. N. C. & Papaloizou, J. 1979, *MNRAS*, 186, 799
- Liu, B., Lambrechts, M., Johansen, A., & Liu, F. 2019, *A&A*, 632, A7
- Liu, B., Lambrechts, M., Johansen, A., Pascucci, I., & Henning, T. 2020, *A&A*, 638, A88
- Lodders, K. 2003, *ApJ*, 591, 1220
- Lubow, S. H., Papaloizou, J. C. B., & Pringle, J. E. 1994, *MNRAS*, 267, 235
- Luque, R. & Pallé, E. 2022, *Science*, 377, 1211
- Lynden-Bell, D. & Pringle, J. E. 1974, *MNRAS*, 168, 603
- Marschall, R. & Morbidelli, A. 2023, *A&A*, 677, A136
- McDonald, G. D., Kreidberg, L., & Lopez, E. 2019, *ApJ*, 876, 22
- Morbidelli, A., Bitsch, B., Crida, A., et al. 2016, *Icarus*, 267, 368
- Mori, S., Bai, X.-N., & Okuzumi, S. 2019, *ApJ*, 872, 98
- Mori, S. & Okuzumi, S. 2016, *ApJ*, 817, 52
- Mori, S., Okuzumi, S., Kunitomo, M., & Bai, X.-N. 2021, *ApJ*, 916, 72
- Mulders, G. D., Min, M., Dominik, C., Debes, J. H., & Schneider, G. 2013, *A&A*, 549, A112
- Müller, J., Bitsch, B., & Schneider, A. D. 2024, *A&A*, 688, A139
- Nakamoto, T. & Nakagawa, Y. 1994, *ApJ*, 421, 640
- Nakatani, R., Turner, N. J., & Takasao, S. 2024, *ApJ*, 974, 281
- NASA Exoplanet Archive. 2024, Planetary Systems, Version: 2024-09-26, IPAC, [doi:10.26133/NEA12](https://doi.org/10.26133/NEA12)
- Oka, A., Nakamoto, T., & Ida, S. 2011, *ApJ*, 738, 141
- Okuzumi, S. 2025, *PASJ*, 77, 162
- Okuzumi, S., Takeuchi, T., & Muto, T. 2014, *ApJ*, 785, 127
- Okuzumi, S., Ueda, T., & Turner, N. J. 2022, *PASJ*, 74, 828
- Ormel, C. W. & Liu, B. 2018, *A&A*, 615, A178
- Owen, J. E., Clarke, C. J., & Ercolano, B. 2012, *MNRAS*, 422, 1880
- Owen, J. E. & Wu, Y. 2013, *ApJ*, 775, 105
- Owen, J. E. & Wu, Y. 2017, *ApJ*, 847, 29
- Paardekooper, S.-J., Baruteau, C., Crida, A., & Kley, W. 2010, *MNRAS*, 401, 1950
- Paardekooper, S.-J., Baruteau, C., & Kley, W. 2011, *MNRAS*, 410, 293
- Parc, L., Bouchy, F., Venturini, J., Dorn, C., & Helled, R. 2024, *A&A*, 688, A59
- Parviainen, H., Luque, R., & Palle, E. 2024, *MNRAS*, 527, 5693
- Perez-Becker, D. & Chiang, E. 2011, *ApJ*, 735, 8
- Pichierri, G., Bitsch, B., & Lega, E. 2023, *A&A*, 670, A148
- Pichierri, G., Bitsch, B., & Lega, E. 2024, *ApJ*, 967, 111
- Picogna, G., Ercolano, B., Owen, J. E., & Weber, M. L. 2019, *MNRAS*, 487, 691
- Raymond, S. N., Quinn, T., & Lunine, J. I. 2005, *ApJ*, 632, 670
- Rogers, J. G., Dorn, C., Aditya Raj, V., Schlichting, H. E., & Young, E. D. 2025, *ApJ*, 979, 79
- Rosotti, G. P. 2023, *New A Rev.*, 96, 101674
- Sano, T. & Stone, J. M. 2002, *ApJ*, 570, 314
- Sato, T., Okuzumi, S., & Ida, S. 2016, *A&A*, 589, A15
- Savvidou, S., Bitsch, B., & Lambrechts, M. 2020, *A&A*, 640, A63
- Schäfer, U., Yang, C.-C., & Johansen, A. 2017, *A&A*, 597, A69
- Shakura, N. I. & Sunyaev, R. A. 1973, *A&A*, 24, 337
- Shibata, K. & Uchida, Y. 1986, *PASJ*, 38, 631
- Sicilia-Aguilar, A., Henning, T., & Hartmann, L. W. 2010, *ApJ*, 710, 597
- Stahler, S. W. & Palla, F. 2004, *The Formation of Stars (WILEY-VCH)*
- Suzuki, T. K. & Inutsuka, S. 2009, *ApJ*, 691, L49
- Suzuki, T. K., Ogihara, M., Morbidelli, A., Crida, A., & Guillot, T. 2016, *A&A*, 596, A74
- Tabone, B., Godard, B., Pineau des Forêts, G., Cabrit, S., & van Dishoeck, E. F. 2020, *A&A*, 636, A60
- Tabone, B., Rosotti, G. P., Cridland, A. J., Armitage, P. J., & Lodato, G. 2022, *MNRAS*, 512, 2290
- Takasao, S., Tomida, K., Iwasaki, K., & Suzuki, T. K. 2022, *ApJ*, 941, 73
- Tanaka, H., Takeuchi, T., & Ward, W. R. 2002, *ApJ*, 565, 1257
- Tanigawa, T. & Tanaka, H. 2016, *ApJ*, 823, 48
- Testi, L., Natta, A., Manara, C. F., et al. 2022, *A&A*, 663, A98
- Venturini, J., Guilera, O. M., Ronco, M. P., & Mordasini, C. 2020, *A&A*, 644, A174
- Wang, L. & Goodman, J. 2017, *ApJ*, 847, 11
- Wang, Y., Ormel, C. W., Huang, P., & Kuiper, R. 2023, *MNRAS*, 523, 6186
- Wang, Y., Ormel, C. W., Mori, S., & Bai, X.-N. 2025, *A&A*, 696, A38
- Weder, J., Mordasini, C., & Emsenhuber, A. 2023, *A&A*, 674, A165
- Williams, J. P. & Cieza, L. A. 2011, *ARA&A*, 49, 67

Appendix A: Pebble-to-gas flux ratio from dust transport simulation

To obtain a typical value of the dust-to-gas flux ratio ξ and its evolution, we calculate the dust transport based on a two-population dust model (Birnstiel et al. 2012), as shown in Figure A.1. We here assume a simple gas structure: surface density profile $\Sigma = 1000 \text{ g cm}^{-2} (r/\text{au})^{-0.75} \exp[-(r/100 \text{ au}) - (t/1 \text{ Myr})^{0.5}]$, temperature profile $T = 170 \text{ K} (r/\text{au})^{-0.5}$, viscosity strength $\alpha_v = 10^{-2}$, and turbulent strength/dust diffusivity $\alpha_t = 10^{-4}$. Other parameters are the same as in Section 3.3.1. Figure A.1 shows the simulated dust surface density Σ_d , Stokes number St , and dust-to-gas flux ratio $\xi = \dot{M}_{\text{peb}}/\dot{M}_{\text{acc}}$. Although ξ has the radial dependence, we here simply fit ξ at $r = 1 \text{ au}$, which gives Equation (26). We plot the fitted ξ values on the right panel of Figure A.1.

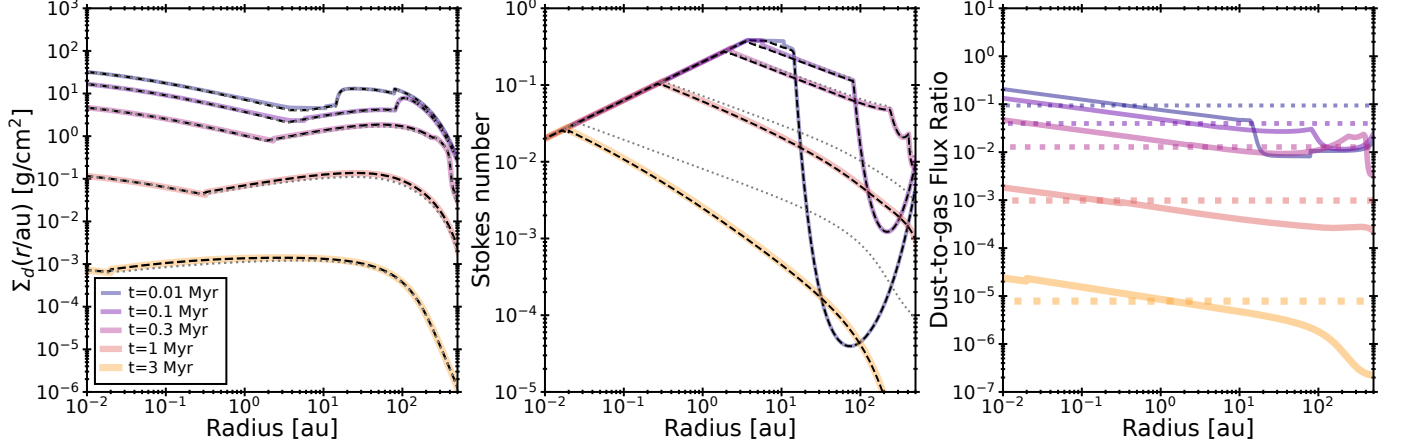


Fig. A.1. Pebble profiles obtained from a two population dust model (Birnstiel et al. 2012, see Appendix A for assumed disk profiles), in comparison with prediction of dust surface density Σ_d and Stokes number for largest dust grains (black dashed; Equation (27)). The classical estimate for St using Equation (B.1) is also shown in the middle panel (gray dotted).

Appendix B: Simple prediction of the pebble Stokes number

We update the classical estimate for the Stokes number of pebbles (i.e., the largest grains) in the radial-drift limit (e.g., Birnstiel et al. 2012; Lambrechts & Johansen 2014), which is given by

$$St_{\text{drift}} = \sqrt{0.55 \frac{|\dot{M}_{\text{peb}}|}{8\pi r \Sigma_g \eta^2 v_K}}. \quad (\text{B.1})$$

However, this expression may break down in the presence of strong gas advection, which determines the dust mass flux (i.e., when $|v_{\text{gas}}| \gtrsim |2\eta v_K|$).

The upper limit of St for the drift limit is obtained by equating the growth timescale with the drift timescale of pebbles. The timescale of pebble drift on a gas comoving frame is written as $\sim r/|r - 2\eta v_K St|$. Meanwhile, the growth timescale is $\sim (\Omega \Sigma_d / \Sigma_g)^{-1}$. Thus, we obtain

$$r/|r - 2\eta v_K St| \sim (\Omega \Sigma_{\text{peb}} / \Sigma_g)^{-1}. \quad (\text{B.2})$$

The pebble mass flux \dot{M}_{peb} is written as

$$\dot{M}_{\text{peb}} = -2\pi r \Sigma_{\text{peb}} (-2\eta v_K St + v_{\text{gas}}) \quad (\text{B.3})$$

for $St < 1$, although some studies here assumed $|v_{\text{gas}}| \ll |2\eta v_K|$. Combining Equations (B.2) and (B.3), we have a quadratic equation of St and obtain:

$$St_{\text{drift}} = \tilde{v}_{\text{gas}} + \sqrt{\tilde{v}_{\text{gas}}^2 + 0.55 \frac{\dot{M}_{\text{peb}}}{8\pi \Sigma_g r v_K \eta |\eta|}}, \quad (\text{B.4})$$

where $\tilde{v}_{\text{gas}} \equiv v_{\text{gas}}/(4\eta v_K)$ and we consider the fitting parameter of Birnstiel et al. (2012). The key point is that the drift timescale should be measured in the gas comoving frame, whereas the pebble mass flux must include the background flow. Once we obtain St , we can calculate the pebble surface density from Equation (B.3).

To demonstrate the obtained formulae, we overplot the analytical expressions for the Stokes number (Equation (27)) and the resulting pebble surface density on the left and middle panels of Figure A.1, respectively. Here, the pebble mass flux is taken from the simulation. We confirm that the formulae accurately reproduce the results of the dust transport simulation. In contrast, the prediction of St using Equation (B.1) deviates from the simulation in the outer region at $t \gtrsim 1 \text{ Myr}$. Note that we adopt a high viscosity in this calculation, which leads to a high gas velocity, causing it to exceed the drift velocity expected from the gas motion.

Appendix C: Dependence of planetary evolution path on parameters

We present planetary evolution tracks for parameter sets other than those in Section 3.3: a case with a lower fragmentation velocity ($v_{\text{frag}} = 1 \text{ m s}^{-1}$) and a case with later onset of protoplanet growth ($t_0 = 0.1 \text{ Myr}$).

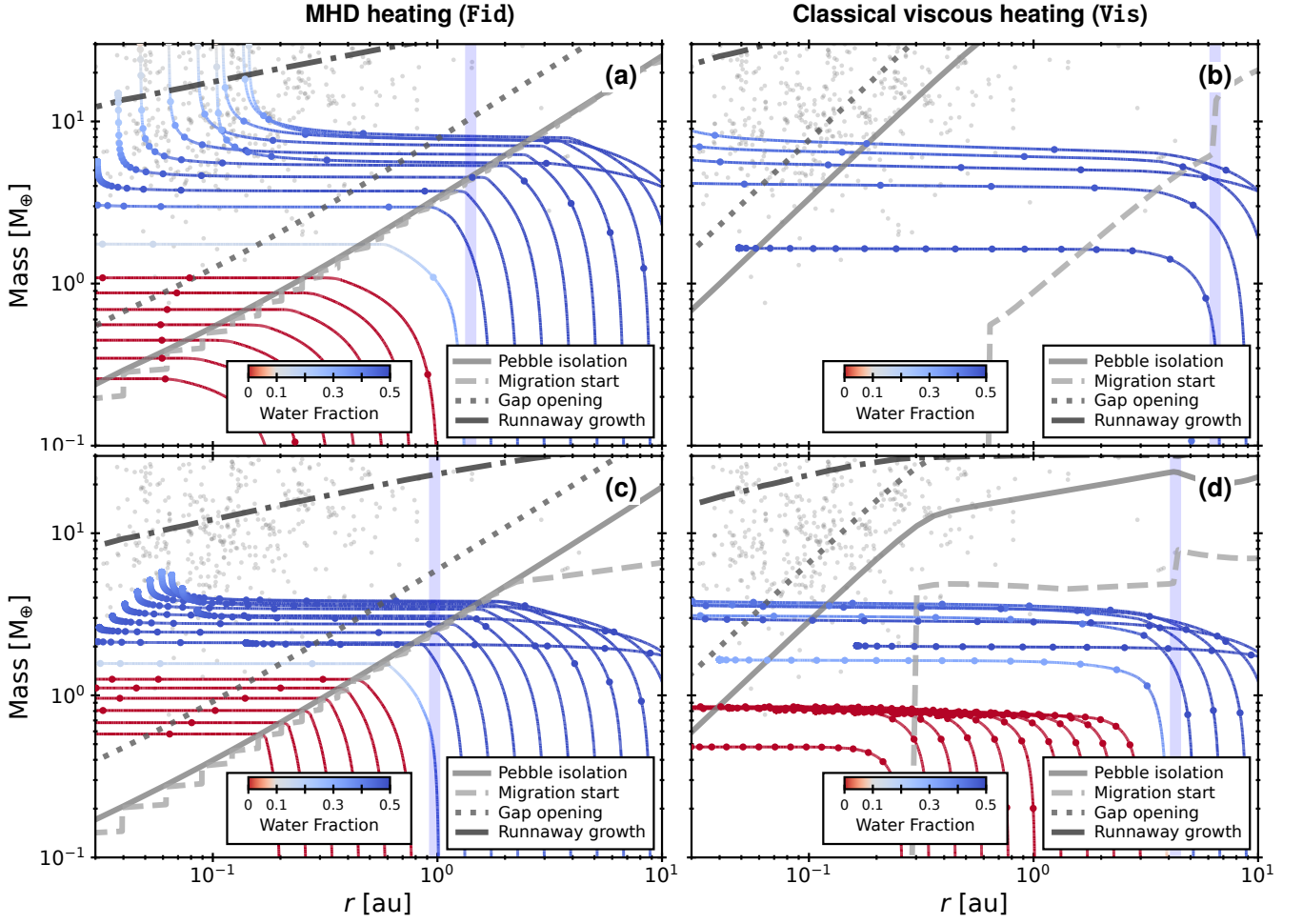


Fig. C.1. Same as Figure 10, but for different parameter sets: (*top*) a case with $t_0 = 0.01 \text{ Myr}$ and $v_{\text{frag}} = 1 \text{ m s}^{-1}$, and (*bottom*) a case with $t_0 = 0.2 \text{ Myr}$ and $v_{\text{frag}} = 10 \text{ m s}^{-1}$. The total drifting pebble masses at the snowline for the former and later cases are $400 M_{\oplus}$ and $100 M_{\oplus}$, respectively.